Coincidence Photon Activation Analysis Using Y-89

A Thesis presented

by

Alison Wells

to

The Department of Physics

in partial fulfillment of the requirements

for the degree of

Master of Science

in the subject of

Physics

Idaho State University

April 2015

To the Graduate Faculty:

The members of the committee appointed to examine the thesis of Alison Wells find it satisfactory and recommend that it be accepted.

_____

Tony A. Forest, Ph.D.,

Major Advisor

_____

Philip L. Cole, Ph.D.,

Committee Member

_____

Chad Pope, Ph.D., P.E.,

Graduate Faculty Representative

To my family.

Acknowledgments

I would like to express my deepest thanks to my advisor, Dr. Forest of the Physics Department, Idaho State University (ISU), for his assistance, encouragement, patience, and support. He has been very important to my success.

I want to thank the Idaho State University Department of Physics and the Idaho Accelerator Center (IAC) professors and staff for their hard work and dedication to their professions. They have helped in the completion of this degree.

A special thanks to my parents and sister for being supportive throughout this process. I could not have done it without you.

Contents

List of Figures

List of Tables

Abstract

This thesis reports on a measurement of the detection limit improvement of coincidence photon activation analysis over the more common Photon Activation Analysis (PAA) for Yttrium (Y-89). PAA is a multi-elemental analysis method capable of quantifying the nuclear isotopes present in materials by activating isotopes of interest and measuring the energy of photons released when the nucleus de-excites. If the isotope of interest de-excites by emitting a cascade of multiple photons, then coincidence photon activation analysis may be used to detect photons that are emitted in coincidence. A foil of natural Yttrium was irradiated at the Idaho Accelerator Center (IAC) using the bremsstrahlung photons produced when a 22 MeV electron beam impinged a 0.3 inch Tungsten target. A coincidence measurement was performed on the activated Yttrium using a HPGe and NaI detector. The measurement found that for every 10^{12} atoms of Y-89, one atom of Y-88 was produced. Coincidence photon activation was able to measure a minimum of 5×10^{18} atoms of Y-89 in the 0.03 g foil improving the detection limit by at least a factor of two over standard PAA.

Key Words: Photon Activation Analysis (PAA), coincidence, Yttrium, detection limit, converting efficiency

Chapter 1

Introduction

Photon Activation Analysis (PAA) is a multi-elemental analysis method that performs photon spectroscopy on materials activated by high energy (MeV) photons to measure the concentrations of elements in a material. The method measures the energy of photons emitted by decaying nuclei using a high purity Germanium detector that has a typical photon energy resolution of 1 keV. Although the observed photon energy may be used to construct a finite list of decaying nuclei, the specific decaying nuclear isotope is usually uniquely identified once a half life is measured. Many activated nuclei de-excite to the ground state by transitioning through several intermediate states and in the process emitting photons within a picosecond or less timescale of each other. This cascade of gamma rays may be used to improve the identification of the decaying nucleus and reduce the background from other decaying nuclei by requiring the detection of at least two photons in coincidence. Coincidence Photon Activation Analysis (CPAA) is a method that requires the detection of at least two photons in coincidence. This thesis quantifies the improvement achieved by CPAA in terms of the lowest number of activated nuclei, the detection limit, that PAA and CPAA can measure.

In addition to PAA, there are several other analytical techniques used

to quantify the elemental composition of materials. They each have their own associated advantages and disadvantages. For example, AAS and ICP methods chemically process a sample, usually by removing a portion of the material and destroying the sample. This is not an ideal technique when investigating materials such as artifacts and antiques, where cutting away pieces for a sample is not desirable. Additionally, there is a danger of introducing contamination during preparation procedures. However, unlike some techniques that are limited to surface studies, these two methods can be used for volume or bulk analysis [1]. Further detailed explanations on some of the more readily available techniques and their differences may be found in Appendix A.

The focus of this thesis is on the detection limits of PAA and CPAA. For comparison, Table 1.1 lists several existing elemental analysis methods along with current detection limits. The detection limits range from 10^{-7} to 100 parts-per-million (ppm) or μg/g. Neutron Activation Analysis (NAA) is one method that is almost identical to PAA, the exception being that a neutron is used to activate a sample instead of a photon. PAA can also provide higher detection power for certain elements [1]. Our particular focus is on improving PAA's detection limit, which currently ranges from 0.01 to 100 ppm [2] [3]. Both NAA and PAA are based upon nuclear interactions in order to activate a target nucleus.

1.1 Nuclear Activation Methods

Nuclei of stable elements can become radioactive when they undergo an inelastic collision that results in the addition or removal of a nucleon or several nucleons from the nucleus. Nuclei are usually left in an unstable state and will almost instantaneously de-excite into a more stable configuration. This process involves the prompt emission of particles or photons. If the initial nucleus to be activated is denoted by $^A_Z X_N$, the incident radia-

2

Table 1.1: Table of Detection Limits

Method	Limit (ppm)
ICP-AES	$10^{-4} \rightarrow 1$
AAS	$1 \rightarrow 100$
PIXE	$0.5 \rightarrow 5$
XRF	$10 \rightarrow 100$
ICP-MS	$10^{-7} \rightarrow 10^{-3}$
NAA	$0.01 \rightarrow 10$
PAA	$0.01 \rightarrow 100$

tion particle as a, and the product nuclide and promptly emitted particles are denoted by ${}^{A'}_{Z'}Y_{N'}$ and b respectively, the reaction can be represented by the equation

$$^{A}_{Z}X_N + a \rightarrow {}^{A'}_{Z'}Y_{N'} + b \tag{1.1}$$
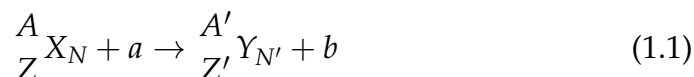
or, in the abbreviated form

$$^{A}_{Z}X_N(a,b)\,{}^{A'}_{Z'}Y_{N'}. \tag{1.2}$$

The type of the nuclear reaction depends upon the target nucleus and the nature and energy of the incident radiation. Many of these product radioactive nuclei decay through β and subsequent γ emission. The γ-rays are characteristic of that particular decay process. By precise determination of the γ-ray energies, it is usually possible to determine not only which isotopes are present, but from the γ intensities it can be determined exactly how much of the original target nucleus was present and consequently the amount of that element present in the sample. The use of neutrons and photons as the activating radiation particle are described below.

3

Neutron Activation Analysis (NAA)

Neutron activation analysis (NAA) is a non-destructive technique used to measure trace elements in materials to within detection limits of $0.01 \rightarrow 10$ ppm [4]. In NAA, the incident radiation particle is a neutron. Several different neutron sources are available, but only a few that offer the high neutron fluxes useful for NAA. These include reactors and accelerators. Since they have high fluxes ($10^{13} \frac{n}{cm^2 \cdot s}$) of neutrons from uranium fission, nuclear reactors offer the highest available fluxes [5]. The sequence of events taking place during the most common type of nuclear reaction for NAA, namely neutron capture (n,γ), is illustrated in Figure 1.1.
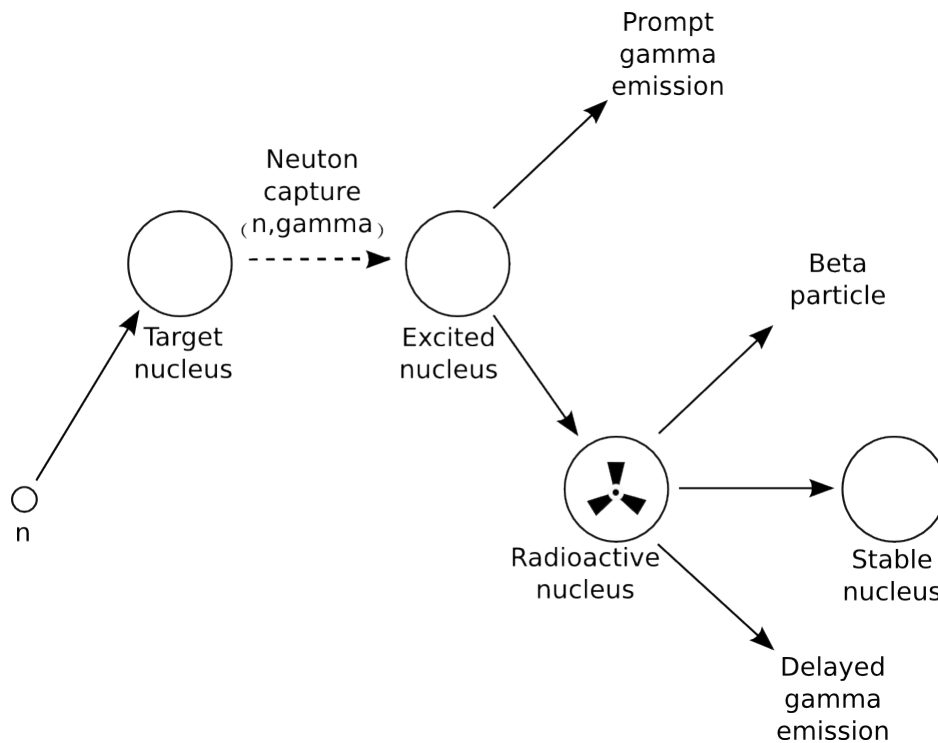
Figure 1.1: Neutron capture process.

Upon irradiation, a neutron is absorbed by the target nucleus. The compound nucleus transitions to an excited and unstable state. This un-

4

stable nucleus de-excites into a more stable configuration by emitting one or more prompt gamma rays. In most cases, this new configuration tends to be a longer lived radioactive nucleus. The newly formed radioactive nucleus now decays by the emission of one or more characteristic delayed gamma rays. The half-life of this decay is unique to the radioactive nucleus. An NAA measurement, in principle, falls into two categories: (1) prompt gamma-ray neutron activation analysis (PGNAA), where measurements are taken during the irradiation of a sample, or (2) the more common delayed gamma-ray neutron activation analysis (DGNAA), where measurements follow radioactive decay. There are several types of detectors employed in NAA. Most are designed to detect the emitted radiation. The detectors most commonly used are scintillation type, with radiation sensitive crystals such as thallium-doped sodium iodide (NaI(Tl)), or semiconductor type detectors. Hyper-pure or intrinsic germanium (HPGe) detectors are the semiconductor type most commonly operated for NAA.

Photon Activation Analysis (PAA)

In photon activation analysis (PAA) [2], nuclei in the sample material are excited into radioactive meta-stable states through exposure to high-energy (MeV) photons. The photon source is typically produced by accelerating electrons onto a target layer of metal with a high atomic number, such as Tungsten. The de-acceleration of electrons passing through the target (radiator) produces electromagnetic radiation. Such radiation is referred to as bremsstrahlung radiation. If the bremsstrahlung radiation strikes a sample nucleus and results in the removal of a nucleon from the nucleus, the nucleus will more often than not be left in an excited state. The resulting nucleus is usually unstable and de-excites by emitting beta or gammas. The energy of the emitted γ radiation is usually characteristic of the nuclide. A measurement of the gamma energy can thus be used to identify the nuclear isotope. Similar to NAA, gamma radiation is commonly mea-

sured with radiation sensitive crystals, such as thallium-doped sodium iodide (NaI(Tl)), or semiconductor type, such as HPGe detectors. For coincidence photon activation analysis, two detectors are used to require the detection of two photons decaying in coincidence.

Concerning the choice of sample that would be activated for PAA study, it was desirable to activate an isotope with half-lives of days to allow measurements of coincidence high and low energy gamma lines. Photon spectroscopy suffers from an increase in background noise when the photon energy decreases below 1 MeV. A detector system can require the presence of two photons from the decay in coincidence in order to separate low energy photon signals from the background noise. From the resources conveniently available, Yttrium met the high and low energy line requirements and had some additional characteristics that were favorable for testing. The half-life of activated Yttrium (Y-88) is 106.63 days. Photon activated materials with such long half-lives allow a waiting period for the short lived contaminates to decay away and still have a signal that could be measured. Details of Yttrium activation and decay process are described below.

1.2   Y-89 Activation

The only natural occurring isotope of Yttrium is Y-89. During photon activation of a Yttrium foil, a neutron is removed from the nucleus in a reaction denoted as $^{89}_{39}Y_{50}(\gamma, n)^{88}_{39}Y_{49}$. The resulting Y-88 nucleus is radioactive with a half-life of 106.63 days. Table 1.2 gives the prominent photon energies emitted by an excited Y-88 nucleus. The 898 keV and 1836.1 keV lines have been observed to be the most prevalent with relative intensities of 93.7% and 99.2%. Table 1.3 provides a list of Y-88 photons along with the gammas they are in coincidence with. Note that the 898 keV and 1836.1 keV lines are also in coincidence. This coincidence occurs when the 2734.1

Table 1.2: Y-88 photon lines and intensities [7].

Energy (keV)	Relative Intensity (%)
850.6	0.065
898.042	93.7
1382.2	0.021
1836.063	99.2
2734.0	0.71
3219.7	0.0070

Table 1.3: Y-88 photons and coincidence gammas [6].

Energy (keV)	Coincidence gamma (keV)
850.6	898.042, 1836.063, 2734.0
898.042	850.6, **1836.063**
1382.2	1836.063
1836.063	850.6, **898.042**, 1382.2
2734.0	850.6
3219.7	

keV state, with a 94% branching ratio, makes a transition after 0.7 ps to the 1836.1 keV state, emitting a 898 keV photon. The 1836.1 keV state will decay to the ground state after 0.154 ps and emit a 1836.1 keV photon. A diagram of the photon energies and their transitions can be seen in Figure 1.2. The total lifetime of the transitions is less than a picosecond [6]. For our experimental setup, discussed in section 2.3, the coincidence timing window was set to 200 ns, so for effective purposes the 898 keV and 1836.1 keV photons are considered in coincidence and will be used for our PAA analysis.
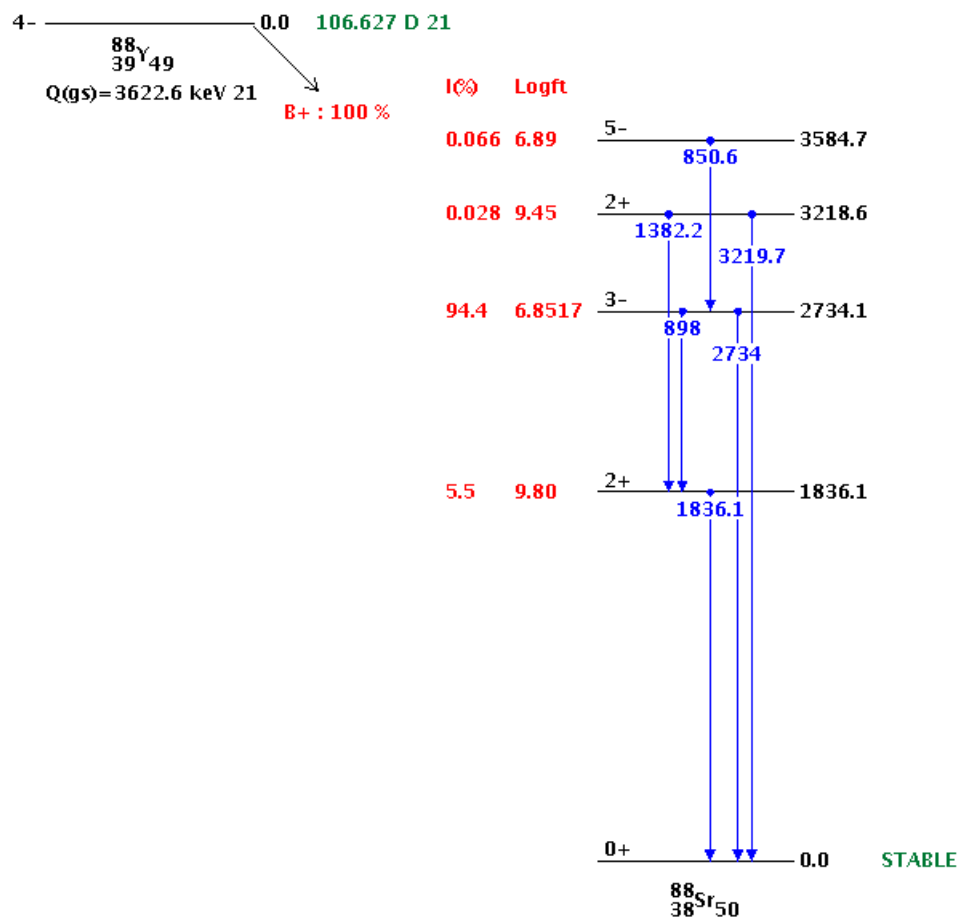
Figure 1.2: Y-88 photon energies and transitions [8].

Chapter 2

Apparatus

2.1 Yttrium Sample Activation Apparatus

Photon activation analysis (PAA) of a Yttrium sample requires the use of an electron accelerator to produce the MeV energy photons used to irradiate the sample and a system of detectors to measure the photons emitted by the post-irradiated sample. Idaho State University's Idaho Accelerator Center (IAC) was used to irradiate the Yttrium sample and perform photon spectroscopy measurements. The IAC's 48 MeV electron linear accelerator (LINAC), commonly referred to as "Jack", was used to accelerate electrons to an energy of 22 MeV. An average electron beam current of 54.4 μA impinged a bremsstrahlung target composed of three 0.100″ thick Tungsten disks as illustrated in Figure 2.1. The three Tungsten disks were separate by 0.150″ to allow water based cooling of the 1.2 kW deposited on the disks by the incident electron beam. A set of target foils were placed 1 m downstream of the Tungsten target to be irradiated by the Bremsstrahlung photons. The Yttrium foil was placed between two nickel foils and attached to a polyethylene block. An additional gold foil was inserted between the nickel foil and polyethylene. Table 2.1 describes the dimensions of the foils used.
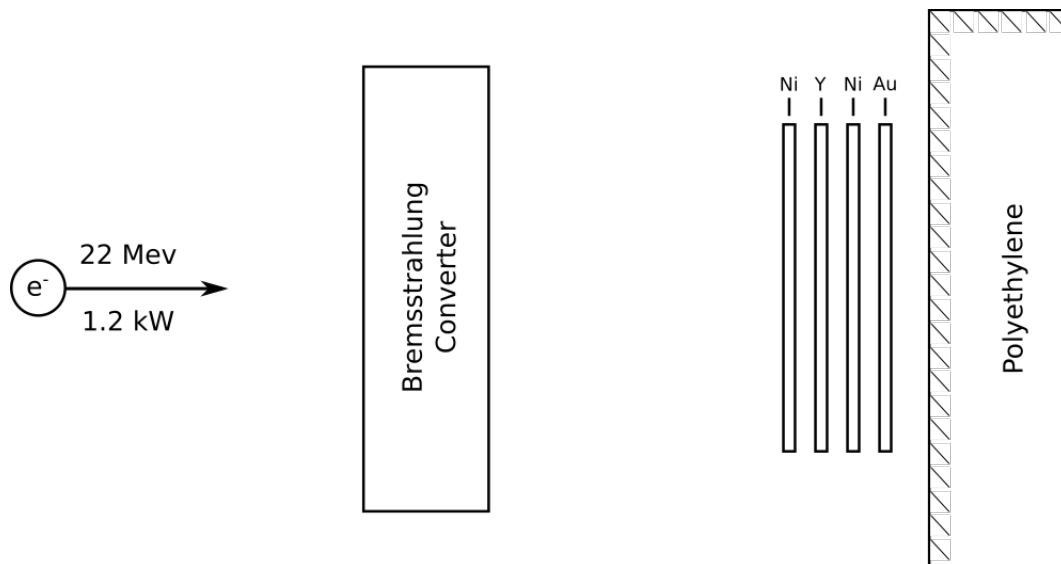
Figure 2.1: Target set-up for photon activation.

Table 2.1: Dimension for foils activated for PAA.

Description	Size (mm)
Width	12.7
Height	19.05
Thickness	0.035

2.2 Coincidence Counting Apparatus

Detectors

HPGe Detector

A high-purity germanium (HPGe) detector is the first of two detectors used in the coincidence set-up. These detectors employ a germanium semiconductor to measure the energy of impinging radiation. In semiconductor detectors, the incident photon's energy is measured by the number of charge carriers set free in the material's valence band and transferred to the conduction band. An equal number of electronic vacancies or "holes" are created in the valance band. Placing the material between two electrodes and applying an electric field will give a measurable charge. In order to reduce thermal excitations of valence electrons, the detector is cooled to liquid nitrogen temperatures. HPGe detectors have an energy resolution of 1 keV [9]. We used a p-type germanium from Ortec model SGD-GEM-50180P-S with an active crystal diameter of 65 mm. The 4600 V detector bias was controlled by the SMART-INTERFACE computer software. Figure 2.2 shows the detector with a dewar attached to keep the detector cool for at least one week before additional nitrogen was required. A diagram of the detector is shown in Figure 2.3.
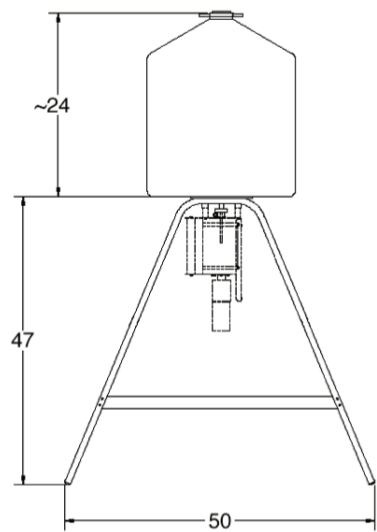
(a) Ortec detector and dewar diagram   (b) Detector B in IAC counting room

Figure 2.2: HPGe detector used for coincidence counting.
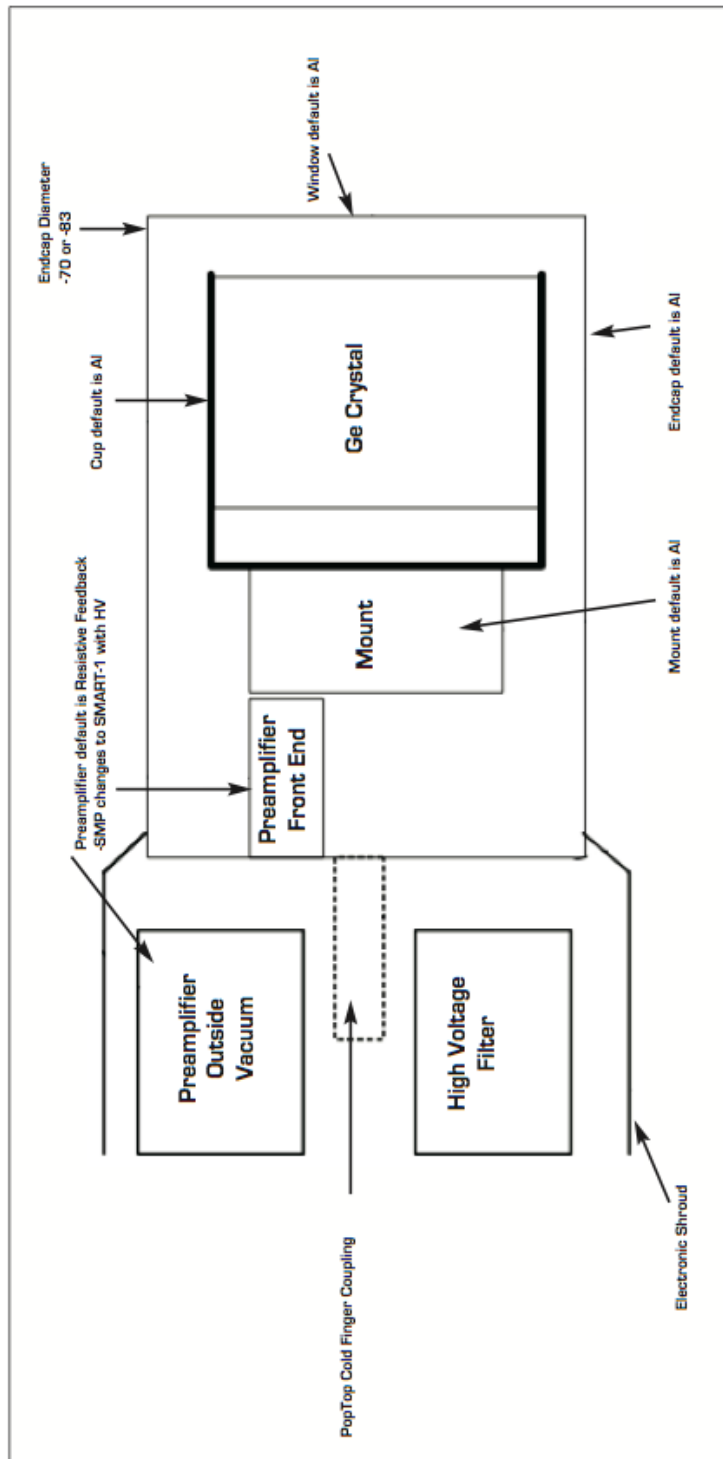
Figure 2.3: HPGe detector internal diagram.

13

NaI Detector

The second detector employed in our coincidence set-up was a Sodium Iodide (NaI) detector. NaI detectors are a type of scintillation detector usually coupled to a photomultiplier tube (PMT). The NaI scintillator material is doped with thallium and scintillates, fluoresces momentarily, when excited by ionizing radiation. Thallium is used to increase the probability for photon emission. The emitted light strikes the PMT's photocathode, releasing at most one photoelectron per photon. The ejected electron is accelerated towards a system of dynodes by an electric field. Additional electrons are knocked off each stage of the dynode due to an applied electric field resulting in a measurable signal that is collected at the anode and coupled to a coaxial BNC output connector [9]. We used a Bicron model 3M3/3 detector with a 3×3 inch crystal. The PMT voltage was set to -1000 V. A picture of the detector and its diagram can be seen in Figures 2.4 and 2.5.

Set-Up Geometry

Samples were positioned on top of polyethylene blocks. The HPGe detector was suspended from a dewar 9.5 cm above the sample. The NaI detector is perpendicular to the HPGe detector and 6.7 cm from the sample. The NaI detector was shielded using two standard ($2 \times 4 \times 8$ inch) Pb bricks. A drawing of the apparatus is shown in Figure 2.6 and Table 2.2 describes the dimensions of the set-up.

Figure 2.4: Sodium Iodine (NaI) detector and parts.

8.75"
(222.3mm)

2.312" dia.
(58.7mm)

3.250" dia.
(82.6mm)

3.187" dia.
(80.9mm)

14 pin phenolic base

Mu-metal
light shield

3" dia. PMT

White
reflector

aluminum housing

NaI(Tl) crystal
3.00 " dia.
X 3.00 " thick
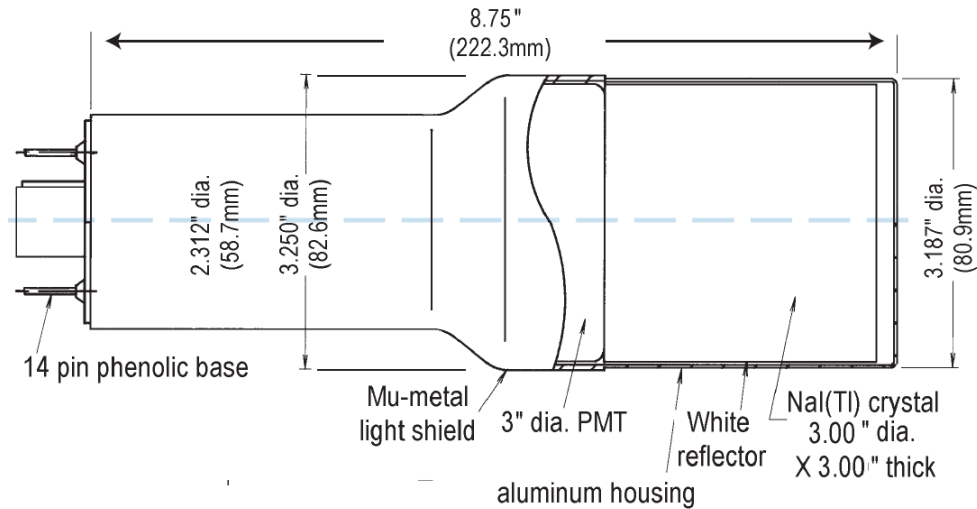
Model 3M3/3

Figure 2.5: NaI detector dimensions.

2.3 Signal Processing

Analog Output

As seen in the HPGe detector diagram in Figure 2.3, the charge carriers from the crystal are sent directly to a preamplifier. This positive voltage signal has a rise time 8 microseconds and a decay time of 60-80 microseconds with an amplitude of 40 mV as shown in Figure 2.7. The signal is next sent to a post amplifier that provides a voltage gain to bring the pulse amplitude to 1.75 V, where it can more conveniently be processed.

The NaI detector PMT output is shown in Figure 2.7. In contrast to the HPGe signal, the negative voltage NaI signal has a pulse width of 2-3 microseconds and an amplitude between 5 and 10 mV. An inverting amplifier was used to convert the signal to a positive amplitude and broaden the pulse with a gradually rounded maximum peak amplitude of 640 mV.

16
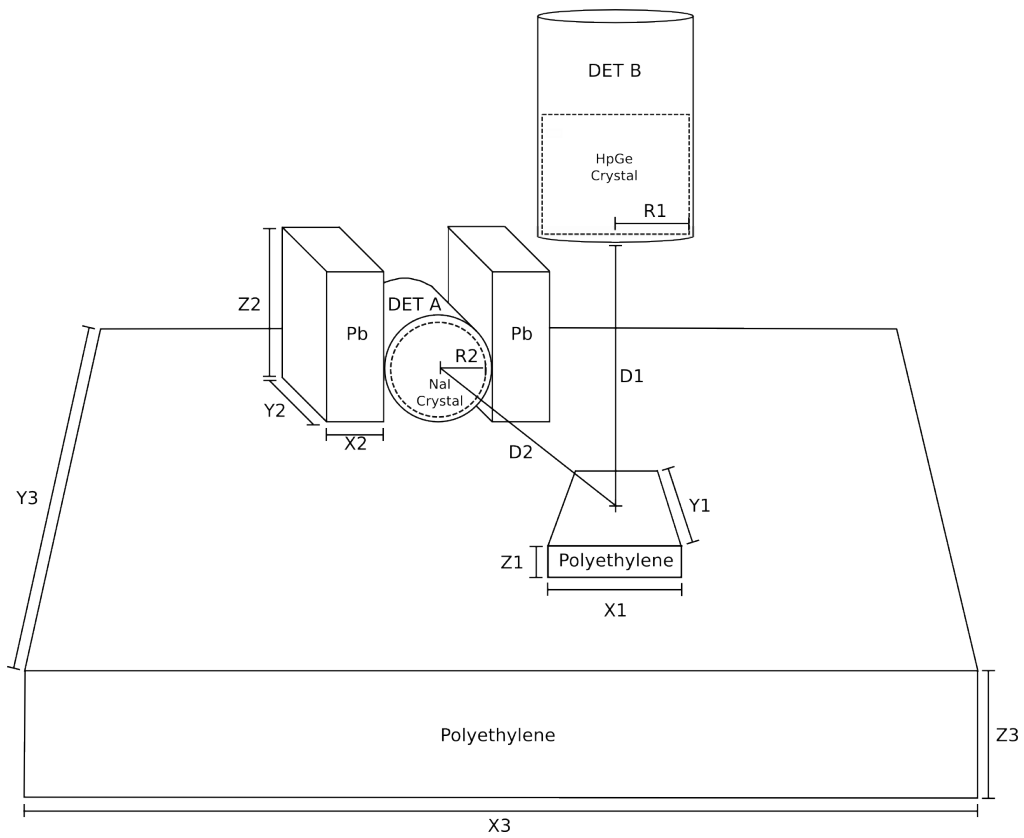
(a) Set-up geometry. Actual dimensions are listed in Table 2.2.
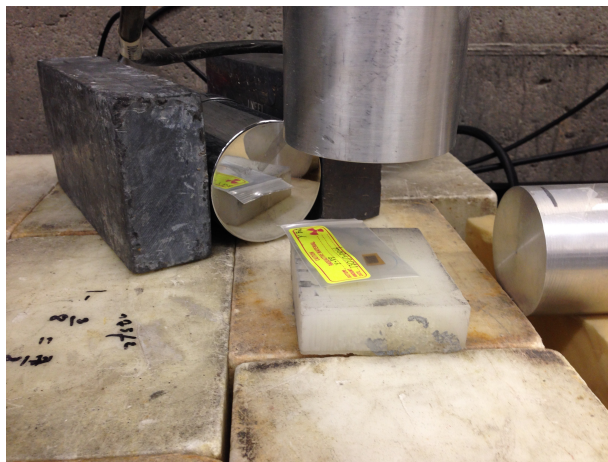
(b) Picture demonstrating sample placement with detectors.

Figure 2.6: Detector set-up and geometry.

Table 2.2: Dimension for detector set-up and geometry as labeled in Figure 2.6.

Description	Size (cm)
X1	7.7
Y1	9.2
Z1	2.5
X2	5.08
Y2	20.32
Z2	10.16
X3	61
Y3	60.5
Z3	41
R1	3.25
R2	3.81
D1	9.5
D2	6.7

The signal is also more symmetric. The amplified signal can be seen alongside the HPGe amplified signal in Figure 2.8.

Analog Signal Processing

Figure 2.9 is a diagram of the analog signal processing modules used for the coincidence experiment. Detector B is positioned directly above the source and corresponds to the HPGe detector mentioned in section 2.2. The pre-amplified signal of the HPGe detector is post amplified by an OR-TEC 673 Spectroscopy Amplifier. The adjustable controls were set to the following values:

> The Spec-Amp course grain was $\times 20$, the fine grain dial was set to $\times 1.04$ for an overall gain of $\times 20.8$, and the sharpening time to 0.25sec. The BLR switch was in the auto position and the input switch in the positive position.
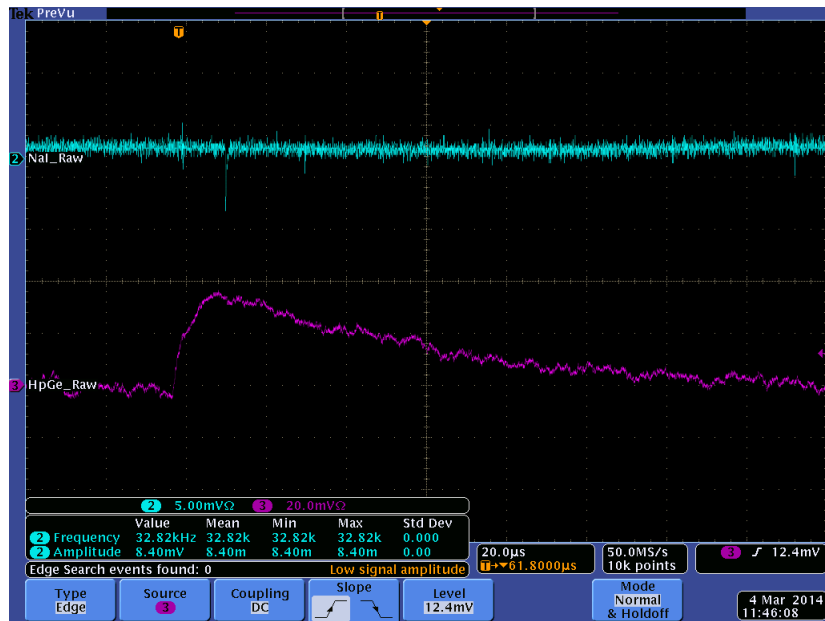
Figure 2.7: NaI and HPGe detector output signals before post amplification.
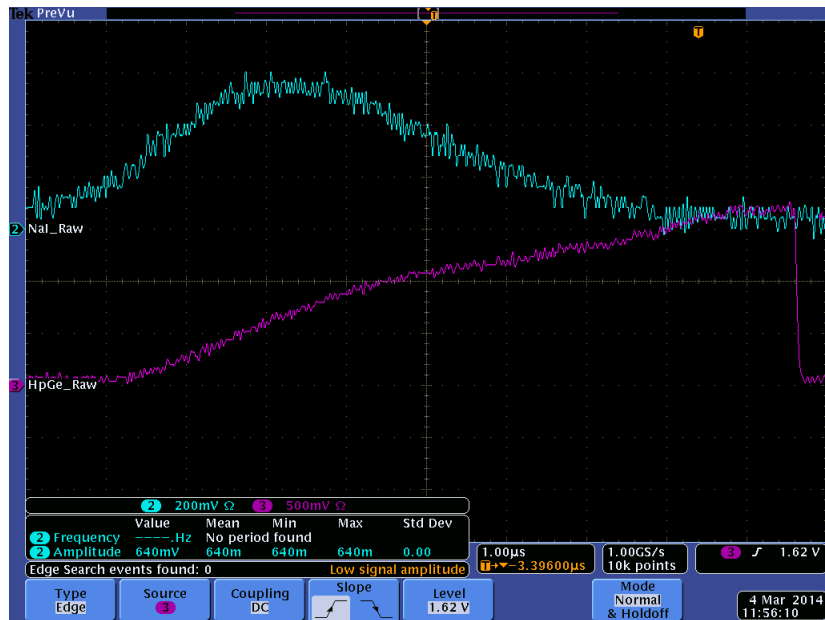
Figure 2.8: NaI and HPGe detector output signals after post amplification.

The time variant gated integrator (GI) output from the Spec Amp goes to a Peak Sensing Analog-to-Digital Converter (PADC) CAEN V785N. The unipolar (UNI) output continues to a Constant Fraction Discriminator (CFD). A NaI detector, detector A, is shown in Figure 2.9. The NaI detector's analog signal also passes through a post amplifier. We used an Ortec 855 Dual Spectroscopy Amplifier in our set-up. The course gain dial was set to $\times 20$ and the fine gain dial was set to $\times 8.98$ for an overall gain of $\times 179.6$. The outgoing signals were sent from the BI output to a CFD and the UNI output to the PADC.
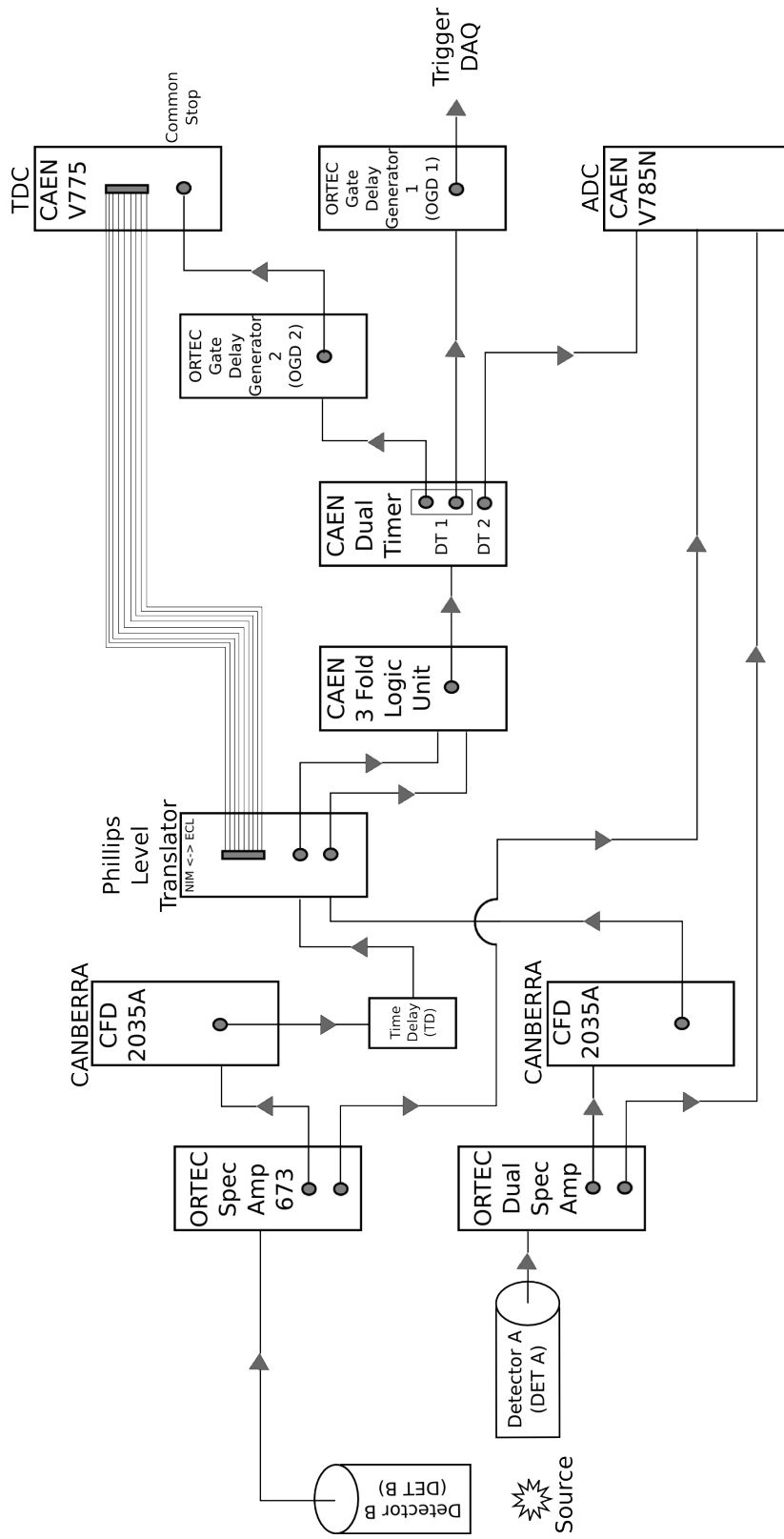
Figure 2.9: Diagram of the modules used for coincidence counting.

21

Discrimination

For our experiment we used two Canberra 2035A Constant Fraction Timing SCAs, which performed both energy and timing analysis on post amplified analog pulses. The amplitude of the analog signal is proportional to the energy a photon deposits in the detector. Low energy background events are reduced using the discriminator. Both CFD modules were set to accept 60 keV photons or greater. The output logic pulse from this constant fraction discriminator occurs at the same point in the rise of the input pulse. To accomplish this, the analog pulse sent into the discriminator is superimposed onto a copy of the same input that has been inverted, attenuated, and offset in time. Adding the two signals yields a bipolar signal. A timing discriminator triggers on the zero-crossing of the signal, producing an output logic pulse. The unipolar output from the CFD with a pulse width of 20 ns went straight to the time-to-digital converter (TDC start). The bipolar output went to two gate generators that were used to increase the pulse width to 100 ns. This increase in the width of the logic pulse corresponds to a 200 ns timing window for coincidence events. In other words, a coincidence exists if the two output signals occur within 200 seconds of each other.

DAQ Readout Timing

The output of the coincidence logic unit is used to trigger the data acquisition system. The trigger was sent into a CAEN Dual Timer with multiple outputs. One output was given a fixed delay (t_{stop}) using an ORTEC Gate Delay Generator before going to the common stop of the TDC. A second pulse, one microsecond wide, was sent to the PADC gate. The analog output from the post amplifiers was delayed in time. This delay was of sufficient length that the amplified analog output was in time with the coincidence logic pulse used to start a measurement in the PADC. A copy of

that same pulse went through a separate gate delay (t_{trig}) and was used to signal the DAQ that data was ready to be readout of the VME modules. The trigger was delayed to allow time for the VME modules to convert the analog signals to digital signals. A diagram of these signals, their widths, and their timing can be seen in Figure 2.10.
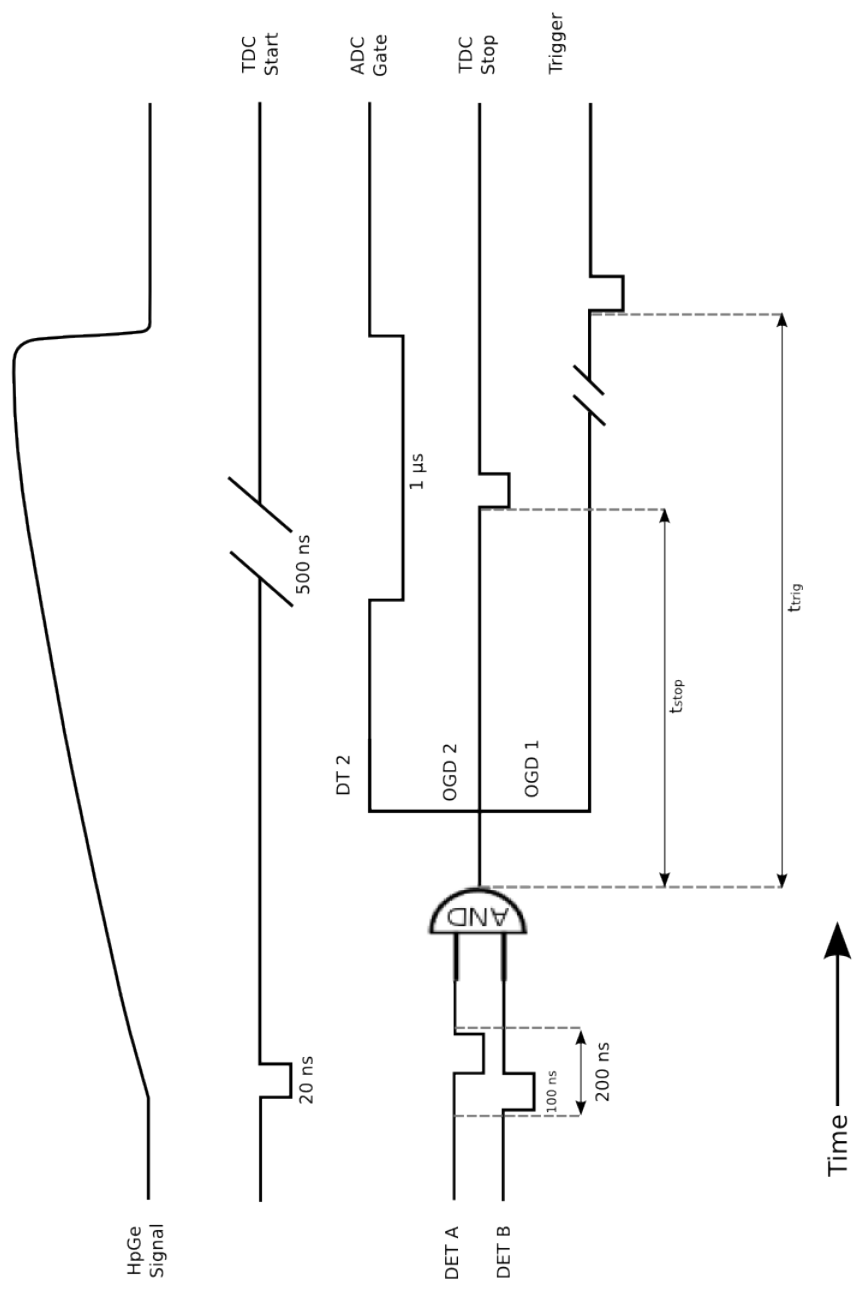
Figure 2.10: Timing diagram of the signals, including from the Dual Timer (DT) and Ortec Gate Delay (OGD). The appatatus operated with the following times: t_{stop}=600 ns, t_{trig}=13 μs.

Coincidence Timing Electronics

The 20 ns wide logic pulses produced by the CFD are sent to a time-to-digital converter (TDC) and to a logic unit, after their width has been increased to 100 ns as shown in Figure 2.10. The logic unit will compare the timing pulses in an AND gate that generates an output if the two pulses are within a 200 nanosecond window. The coincidence output is used to open a linear gate that signals the PADC to look for a peak within a 1 μs window. Figure 2.11 is a plot of the time difference between the two detector pulses thought to be in coincidence. It shows the expected timing window of ± 100 ns. The probability of having a false coincidence is estimated by dividing the number of accidental background events using the number of real coincidence events. The probability of an accidental event was approximately 10.19% for a best case scenario and approximately 24.81% for a worst case scenario.

2.4   Calibrating Detectors

The detectors are calibrated using standard sources of Cs-137, Co-60, Na-22, Ba-133, and Mn-54. The certificates for these sources are located in Appendix B. Each source was counted in singles mode until the number of events had exceeded 100,000. The mean and sigma of each energy peak was recorded and these values along with the known photon energies were fit to a linear function. Table 2.3 gives Ba-133 known energies in column 1, along with an example of the observed PADC channels before calibration given by the HPGe detector. The parameters of the fit were applied to calibrate the detectors. Figure 2.12 shows the Ba-133 energy spectrum before and after the detector was calibrated. The long term variance in detector calibration parameters over the course of experiment and the impact of energy calibration drift is analyzed in section 4.3.
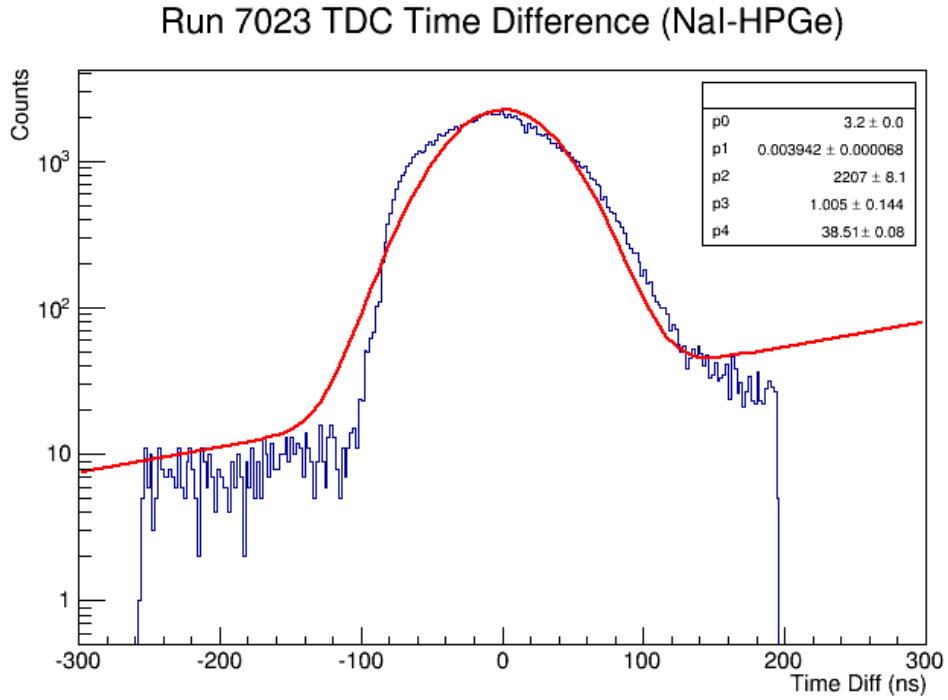
Figure 2.11: Time difference between the NaI detector and the HPGe detector. Equation 4.1 used for fitted curve (red). $\chi^2/ndf = 8245/222$.

Table 2.3: Ba-133 Photon Energies.

Ba-133 Coincidence Photon Energies (keV)	HPGe Energies Before Calibration (channels)
80.9971	220.9 ± 1.81
276.3997	546.6 ± 1.87
302.8510	590.5 ± 1.67
356.0134	678.9 ± 1.52
383.8480	725.1 ± 1.71
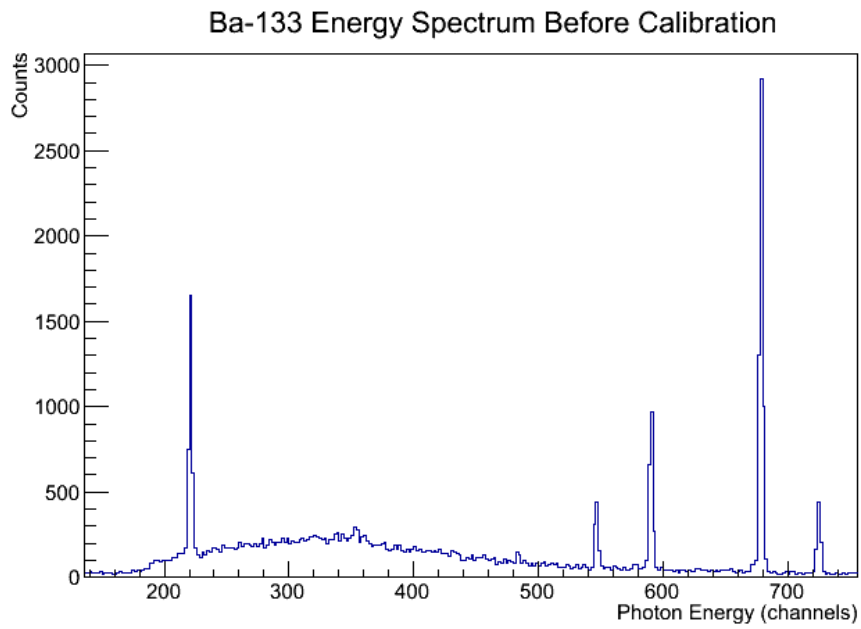
(a) before calibration
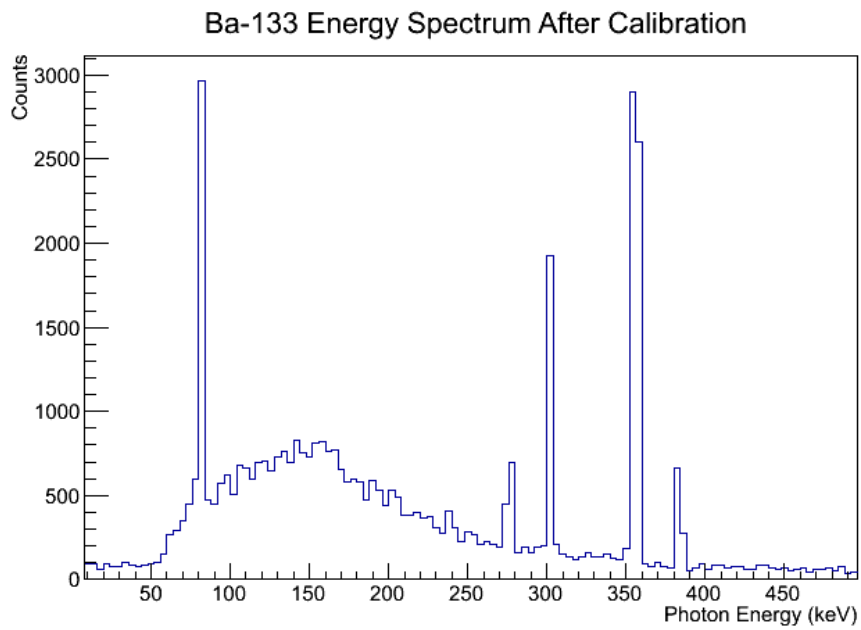
(b) after calibration

Figure 2.12: Ba133 Energy Spectrum.

27

Chapter 3

Data Analysis

After acquiring the spectroscopy spectrum using the apparatus described in Chapter 2, the 898 keV and 1836.1 keV energy lines were analyzed to determine the samples activity as part of PAA. It is important to review some terminology used before proceeding with the analysis process. As shown in Chapter 2, the module set up included a CAEN 3 Fold Logic Unit. This unit allowed data to be collected with an OR or an AND logic requirement. Data collected using the OR gate are referred to as singles events, while data collected with an AND gate are coincidence events.

3.1   Analysis of 898 keV and 1836.1 keV Lines

The 898 keV and the 1836.1 keV are the most prevalent photon energies released in Y-88 decay. Since the total lifetime of the transition states associated with these energies are less than a picosecond, these photons are considered to be in coincidence. The following sections describe the methods used to analyze these energy lines using singles and coincidence counting.

Singles Counting

The Amplitude Method

A simple approach to calculating the detection limit focuses on the amplitude of the energy peaks. Utilizing a data analysis program developed at CERN called ROOT [10], each peak was fit to a Gaussian curve. The fit parameters corresponding to the peak amplitude and its associated error can be found in Table 3.1.

Table 3.1: Peak amplitude values used to calculate the half-life of Y-88 for singles counting using the amplitude method.

Run #	Time After Activation		Energy (keV)	Activity (Hz)
	(Days)	($T_{1/2}$)		
7022	108	1.01	898	1.11421 ± 0.057009
			1836	0.493043 ± 0.040830
7107	159	1.49	898	0.558352 ± 0.044758
			1836	0.265019 ± 0.026870
7235	245	2.30	898	0.434429 ± 0.042097
			1836	0.147541 ± 0.023407

The next step was to investigate background removal from the signal. Background subtraction is an important step to reduce noise or any spectral contribution from materials other than the isotope of interest. A simple method to determine the background involves fitting the sides of the peak to a line with zero slope. The y-intercept gives the background amplitude. A weighed average of the background was calculated to be 0.0255 ± 0.0206 Hz for the 898 keV line and $0.0072 +/- 0.0120$ Hz for the 1836.1 keV line. The error on the background supported the assumption that the noise had died away sufficiently to be consistent with zero. No background was subtracted under the amplitude method for analysis.

The half-life of Y-88 was determined by fitting the time dependence of the measured peak amplitude to the function:

$$A(t) = A_0 e^{(A+Bt)}, \tag{3.1}$$

where A_0 is the initial activity, A is a constant, B is the slope, and t is the time since activation. Taking the inverse of the fitted slope gives the calculated half-life of Y-88. The half-lives of elements are well known [11], which meant the calculated half-life provided a check for the measured activities. Figure 3.1 shows the activities fit to the exponential function (eq. 3.1).

Using the fit parameters obtained from finding the half-life, it is possible to calculate the initial activity (A_0) of the sample after activation. The initial activity is obtained by setting the time equal to zero in the above equation 3.1. The detector efficiency for measuring the Y-88 energy lines needs to be taken into account. In order to do this, the activity was divided by the measured geometrical efficiency (see section 3.2). This will give the absolute activity of the foil.

Using the relationship between activity and the number density:

$$A_0 = \lambda N_0 \tag{3.2}$$

where λ is the decay constant, we can calculate N_0 for t=0. This value used the known half-life of Y-88, rather than the half-life obtained from fits. There should be agreement between the values of A_0 and N_0 found using the 898 keV and 1836.1 keV energy lines. The initial number of radioactive nuclei (N_0) was calculated to be $(40.57 \pm 7.33) \times 10^8$ nuclei for the 898 keV line and $(54.71 \pm 6.41) \times 10^8$ nuclei for the 1836.1 keV line, an agreement to within almost one standard deviation.

The next property of interest is the signal to noise ratio (SNR) for the purpose of determining the detection limit. It is preferred to know how long measurements can be taken before the signal is no longer identifiable from the noise, or our SNR is effectively zero. The peak amplitudes are di-
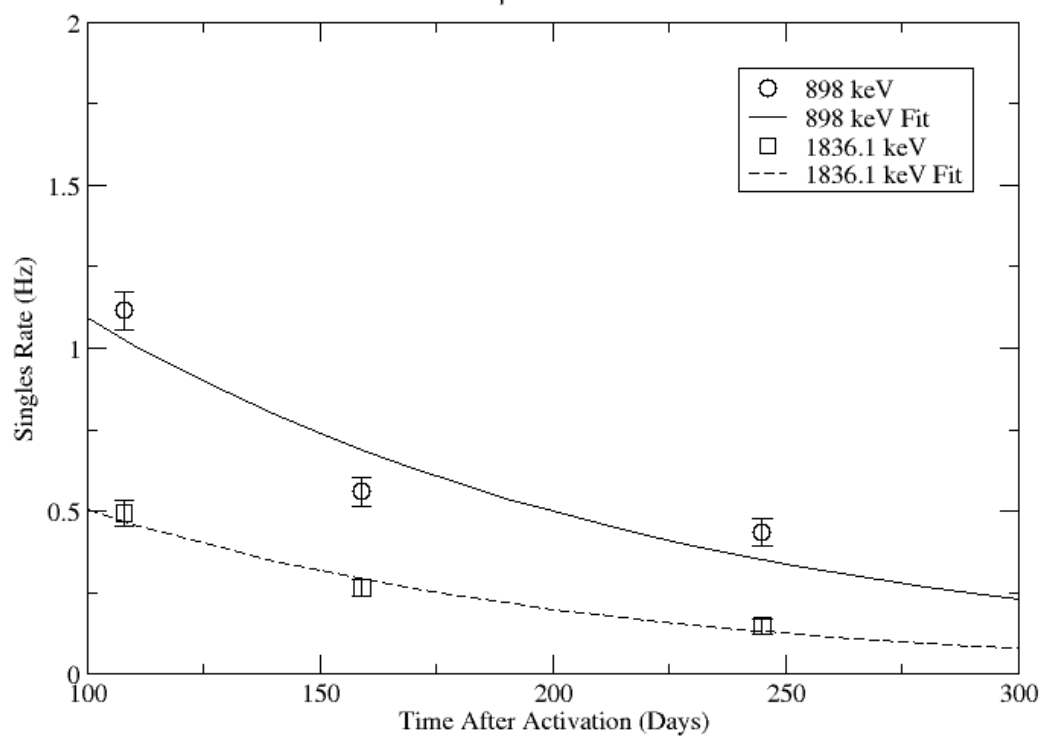
Figure 3.1: Singles signal peak amplitudes for 898 keV and 1836.1 keV energies fitted to an exponential curve. Rates have not been corrected for detector efficiency. Uncertainties are statistical.

vided by the weighted average background and fit to a line. The linear fit is extrapolated to where it crosses the x-axis to find the time (t_{final}) when measurement is no longer feasible. Table 3.2 lists the values obtained for the signal to noise ratio, and Figure 3.2 plots these values and the corresponding fit.

Table 3.2: Signal to Noise Ratio values, for singles counting, obtained by dividing the peak amplitude by the background.

Run #	Time After Activation		Energy (keV)	SNR
	(Days)	($T_{1/2}$)		
7022	108	1.01	898	43.69 ± 2.24
			1836	68.48 ± 5.67
7107	159	1.49	898	21.90 ± 1.76
			1836	36.81 ± 3.73
7235	245	2.30	898	17.04 ± 1.65
			1836	20.49 ± 3.25

Since the initial values A_0 and N_0 have been determined along with a final time, the decay equations

$$A(t) = A_0 e^{-\lambda t} \tag{3.3}$$

$$N(t) = N_0 e^{-\lambda t} \tag{3.4}$$

can be utilized to find the final activity and number of radioactive nuclei that can be measured by the set-up. It was calculated from the 898 keV data that $A(t_{final}) = 34.09 \pm 19.05$ Hz and $N(t_{final}) = (4.53 \pm 2.53) \times 10^8$ nuclei. The 1836.2 keV data found $A(t_{final}) = 55.38 \pm 8.74$ Hz and $N(t_{final}) = (7.36 \pm 1.16) \times 10^8$ nuclei. A full summary of the results is located in section 3.3.
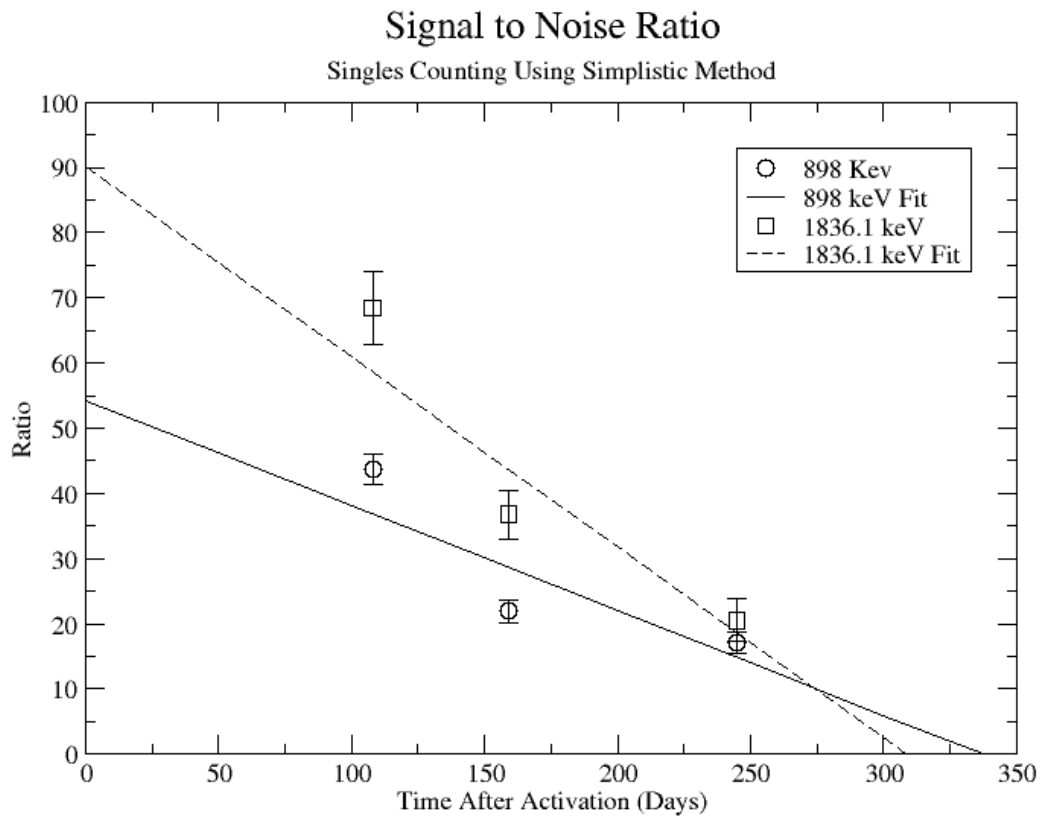
Figure 3.2: Singles signal to noise ratios with linear fit used to extrapolate t_{final}.

The Integral Method

A more complicated method of analysis involves finding the integral of the energy peak by first subtracting the underlying background. It should be noted that during the analysis of the third data point collected, measured 229 days after activation, significantly smaller activity was measured. Upon reviewing calibration runs taken on the same days as the Yttrium measurements, it was discovered that there was an unknown error affecting the system that particular day. While this third point could be artificially boosted based on the known half-life of yttrium and has been included in some plots and tables presented later, it has been excluded from all data fits related to half-life. The background was determined by fitting the observed window with a function that was a combination of a gaussian curve and a line. The linear fit parameters were entered into a simple program read into ROOT that subtracted the background from the histogram. An example of this ROOT script is located in Appendix C. The remaining signal was integrated to find the area under the peak. The values were fit to an exponential curve to obtain a calculated half-life ($T_{1/2}$), activity (A), and number density (N) using the same approach outlined in the previous section. Figure 3.4 shows this fit. The SNR was calculated by dividing the background subtracted signal integral by the integrated area of the background.

The data points where subjected to a linear fit and the time t_{final} was extrapolated. The first data point for the singles 898 keV line was much smaller and not included in the SNR fit. At the time of measurement, the background noise appeared to be larger and decreases the value of the ratio. This could be from contaminants with short half-life in the sample that later decayed away. Only elements with longer half-lives, such as Y-88, remained for the later data points. The backgrounds of the remaining three data points were averaged for the fit. Figure 3.5 plots the SNR values and shows the extrapolated fit.

Looking for agreement between the initial values A_0 and N_0 for the 898 keV and the 1836.1 keV lines showed that they differed by a factor of 2. This integral method fails for single counting. The main contributor to this method failing is believed to be the background. The simple method predicts initial values for A_0 and N_0, which are all consistent. The integral method could be giving too much weight to the zero background and driving the initial number of nuclei from agreement.

Coincidence Counting

Using our Y-88 source, our set-up allows us to perform runs with the detectors in coincidence (AND mode) or singles (OR mode). Figure 3.3(a) shows the HPGe detector's coincidence events (red) that occurred within a 200 ns timing window. This graph has been overlaid with the same detector's singles events (blue). We can see that by having the detectors in coincidence, the noise is reduced and several peaks, which do not have multiple photons in coincidence, are removed.

The coincidence data does not show the two energy peaks associated with Y-88 decay alone. Even though we require coincidence for the system to trigger, there is still noise. Those events could be coincidence events where the photon has lost energy due to Compton scattering. Photons can lose a portion of their energy traveling to the detector, but calibration accounts for this loss. They do not necessarily have to deposit all of their energy into the detector either. The photon can Compton scatter out of the detector. It is not possible to tell the difference between a photon that deposited all of its energy from one that scattered with this apparatus. The photons can, however, be distinguished if an energy cut is applied. In order to remove the Compton events and the accidentals, we can require the photon energy to be completely deposited into the detector. This can be achieved by placing an energy cut on the photons detected by one of the detectors. Figure 3.3(b) is an overlay of the coincidence signal before

(blue) and after (red) an energy cut is applied to the companion detector (NaI detector). The noise seen at low energies is greatly reduced after including the cut.

After applying the energy cut to the NaI detector's appropriate energy line, the data was analyzed using the integral method described in the previous section. Figure 3.4 shows the integral values and exponential fit results for the integral method for singles and coincidence method. It should be noted that for the 898 keV signal to noise fit, the last data point was not included. The extended length of the run, over several days, and activities in the counting room during counting, such as refilling of the nitrogen tank, caused the peak to spread over a larger energy range. This affected the integrated area under the peak, as well as the area of the background noise, to be larger than expected. The backgrounds of the remaining three points were averaged to determine the SNR. These SNR fits and points can be seen in Figure 3.5 for both singles and coincidence counting. Tables 3.3 and 3.4 give the data used to obtain the fits. It was calculated from the 898 keV data that $A(t_{final}) = 39.35 \pm 9.51$ Hz and $N(t_{final}) = (5.23 \pm 1.26) \times 10^8$ nuclei. The 1836.2 keV data found $A(t_{final}) = 137.59 \pm 29.78$ Hz and $N(t_{final}) = (18.29 \pm 3.96) \times 10^8$ nuclei. The N_0 values for coincidence analysis were self consistent using the integral method. Comparing these results with the values for N_0 found in section 3.1, the initial number of nuclei in the foil are in agreement for singles and coincidence counting . A summary of the results is located in section 3.3.
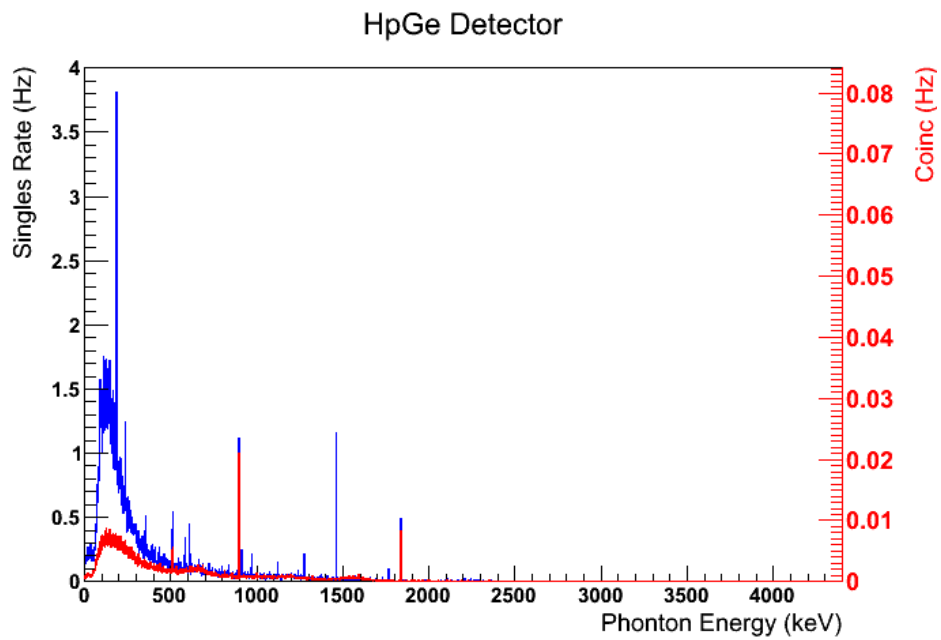
(a) Coincidence events (red) and Singles events (blue) overlayed.
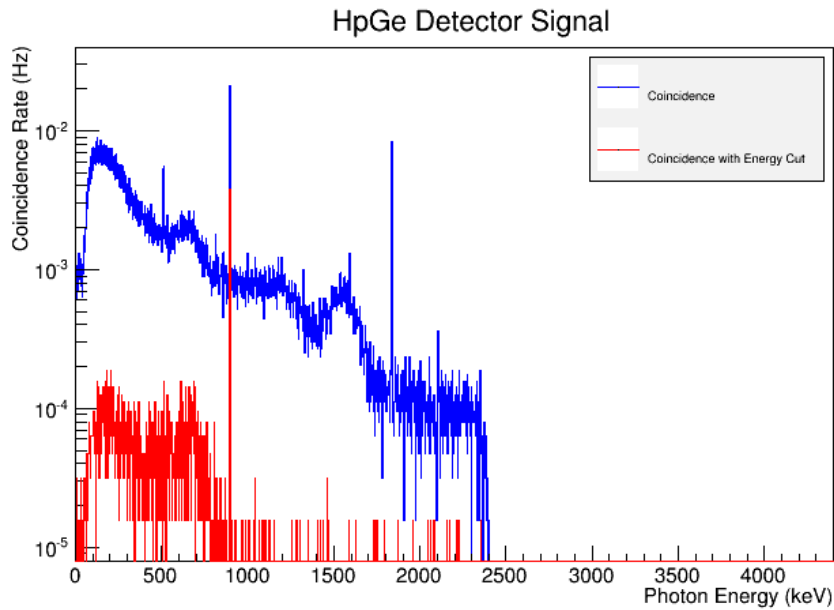
(b) Before energy cut (blue) and after energy cut (red) overlayed.

Figure 3.3: Energy spectrum demonstrating noise reduction techniques.

Table 3.3: Integral values use to calculate the half-life of Y-88 for coincidence counting using the integral method.

Time After Activation (Days)	$(T_{1/2})$	Energy (keV)	Integral	Statistical Error	Systematic Error	Systematic Error (No Energy Cut)
108	1.01	898	0.0052	$\pm\, 2.864 \times 10^{-4}$	$+6.39\times10^{-4}$ -1.8×10^{-3}	$+1.86\times10^{-4}$ -1.84×10^{-4}
		1836.1	0.0062	$\pm\, 3.13 \times 10^{-4}$	$+3.91\times10^{-4}$ -2.64×10^{-3}	$+1.14\times10^{-4}$ -1.11×10^{-4}
159	1.49	898	0.0042	$\pm\, 2.263 \times 10^{-4}$	$+4.43\times10^{-4}$ -6.45×10^{-4}	$+8.3\times10^{-5}$ -7.82×10^{-5}
		1836.1	0.0046	$\pm\, 2.37 \times 10^{-4}$	$+4.98\times10^{-4}$ -2.87×10^{-3}	$+6.66\times10^{-5}$ -7.43×10^{-5}
229	2.15	898	0.0034	$\pm\, 2.587 \times 10^{-4}$	$+5.62\times10^{-4}$ -1.24×10^{-3}	$+1.41\times10^{-4}$ -2.17×10^{-4}
		1836.1	0.0062	$\pm\, 4.60 \times 10^{-4}$	$+1.29\times10^{-3}$ -6.07×10^{-3}	$+2.39\times10^{-4}$ -3.63×10^{-4}
245	2.30	898	0.0015	$\pm\, 5.454 \times 10^{-5}$	$+3.68\times10^{-4}$ -1.53×10^{-3}	$+1.27\times10^{-5}$ -1.47×10^{-5}
		1836.1	0.0016	$\pm\, 5.63 \times 10^{-5}$	4.72×10^{-4} -1.23×10^{-3}	$+1.20\times10^{-4}$ -1.21×10^{-4}

Table 3.4: Signal to noise ratio values used to calculate t_{final} for coincidence counting using integral method.

Time After Activation		Energy (keV)	SNR	Statistical Error	Systematic Error
(Days)	($T_{1/2}$)				
108	1.01	898	46.181	$\pm 4.204(9.10\%)$	$^{+1.653}_{-1.635}$
		1836.1	40.666	$\pm 1.236(3.04\%)$	$^{+0.748}_{-0.728}$
159	1.49	898	37.30	$\pm 1.132(3.03\%)$	$^{+0.739}_{-0.694}$
		1836.1	30.172	$\pm 2.480(8.22\%)$	$^{+0.437}_{-0.489}$
229	2.15	898	30.195	$\pm 2.480(8.21\%)$	$^{+1.253}_{-1.926}$
		1836.1	40.666	$\pm 3.095(7.61\%)$	$^{+1.566}_{-2.379}$
245	2.30	898	37.994	$\pm 4.287(11.28\%)$	$^{+0.322}_{-0.372}$
		1836.1	0.7569	$\pm 0.057(7.57\%)$	$^{+0.0568}_{-0.0572}$

3.2 Efficiencies

Singles Efficiency

A measurement of the HPGe detectors geometric efficiency for detecting the Y-88 energy lines at 898 keV and 1836.1 keV was performed in order to determine the absolute activity of the sample. The count rate for several sources of known activity was measured using the data acquisition system. Since each sample has decayed since the original calibration by the source vendor, column 4 of Table 3.5 reports the expected rates from each calibrated sample that were calculated using the half life and the known activity of the standard sources. The characteristic energy peaks from each source was fit to a gaussian distribution. The variance from that fit was used to determine the range of integration for the count rate measurement. The integration energy range was selected to include counts over the energy interval from $\bar{E} - 2\sigma$ to $\bar{E} + 2\sigma$. The measured rates for each calibrated source using the HPGe detector are listed in column 5. The efficiency given by the ratio of the rates in column 5 to the expected rates
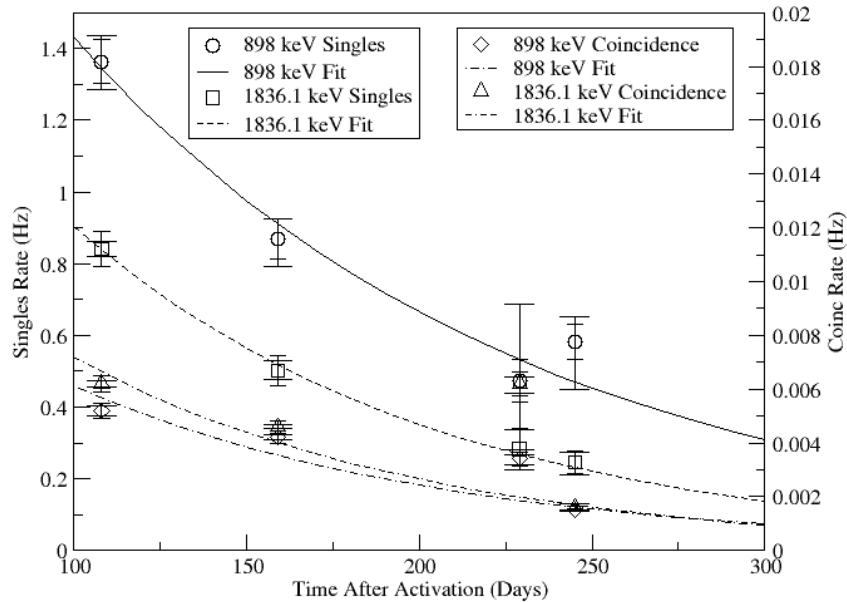
Figure 3.4: Integral values fit to exponential curves for singles and coincidence counting using the integral method.

in column 4 are shown in column 6 of the same table. The percent efficiency of the standard sources was fit to a exponential curve shown in Figure 3.6(a). The singles efficiency for 898 keV and 1836.1 keV were extrapolated from the exponential equation and are recorded in Table 3.7. This process was repeated for the NaI detector and the results can be seen in Figure 3.6(b) and Tables 3.6 and 3.8.
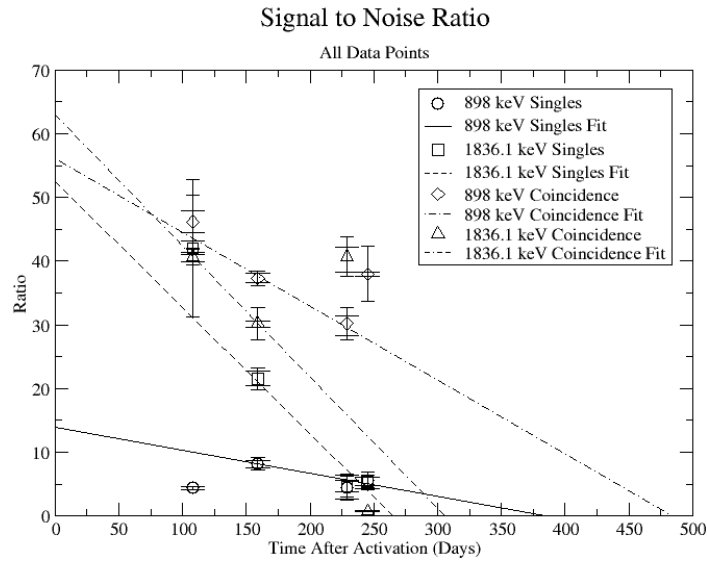
(a) SNR plot showing all data points
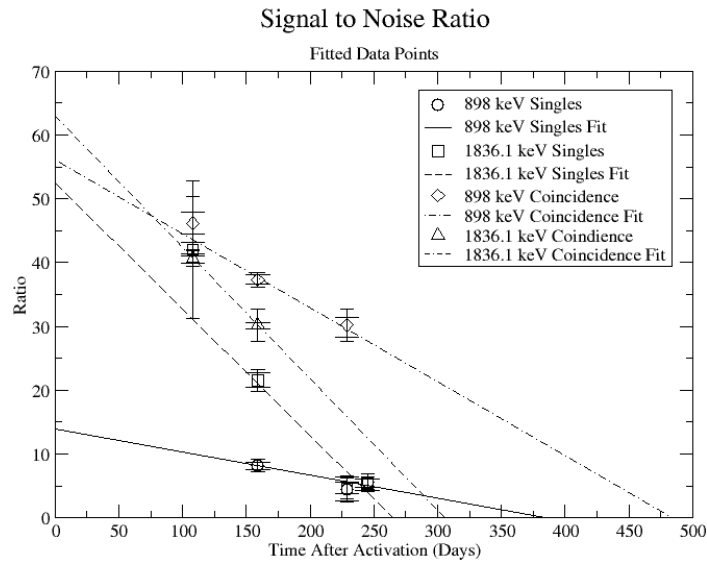
(b) SNR plot showing fitted data points

Figure 3.5: Coincidence signal to noise ratio with linear fits used to extrapolate time t_{final} for singles and coincidence counting using a integral method.
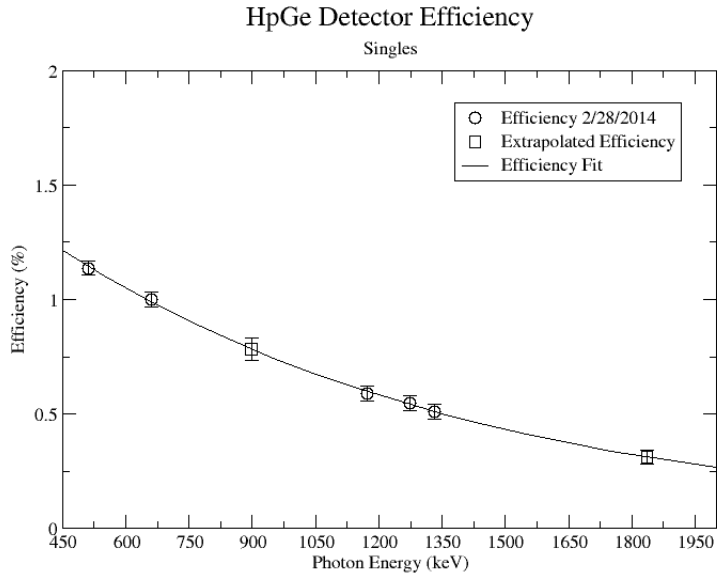
(a) HPGe Detector
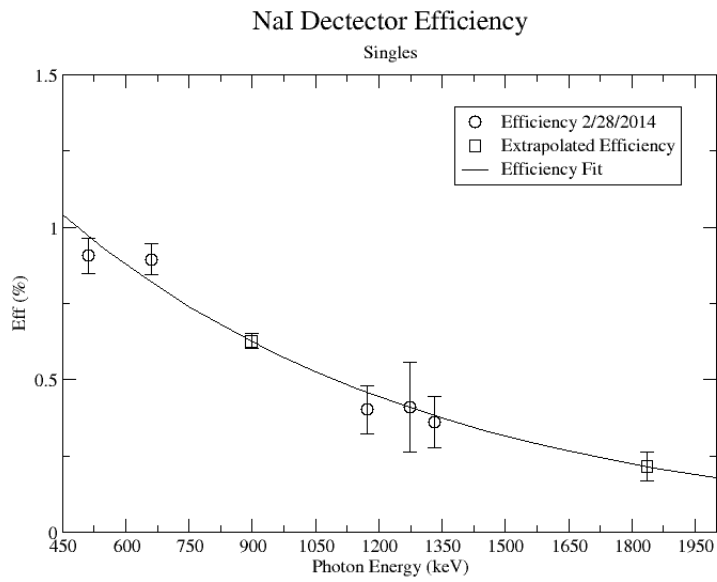
(b) NaI Detector

Figure 3.6: Detector effeciency as a function of photon energy.

Table 3.5: HPGe Detector Rates and Effeciencies.

Run	Source	Energy	Expected Rate (Hz)	HPGe Det B Rate (ADC 7) (Hz)	HPGe Eff (%)
7027	Na-22	511	1589.218 ± 49.425	18.07 ± 0.111	1.137 ± 0.0317
7025	Cs-137	661.657	2548.03 ± 80.008	25.468 ± 0.172	0.9995 ± 0.0321
7029	Mn-54	834.848	41.405 ± 1.300	0.485 ± 0.014	1.171 ± 0.0427
7026	Co-60	1173.228	1876.619 ± 58.926	11.03 ± 0.106	0.588 ± 0.0328
7027	Na-22	1274.537	888.264 ± 27.625	4.857 ± 0.034	0.5468 ± 0.0319
7026	Co-60	1332.492	1878.167 ± 58.974	9.584 ± 0.023	0.510 ± 0.0315

Table 3.6: NaI Detector Rates and Effeciencies.

Run	Source	Energy	Expected Rate (Hz)	NaI Det B Rate (ADC 3) (Hz)	HPGe Eff (%)
7027	Na-22	511	1589.218 ± 49.425	14.393 ± 0.715	0.9057 ± 0.0586
7025	Cs-137	661.657	2548.03 ± 80.008	22.8 ± 0.9154	0.8948 ± 0.0510
7026	Co-60	1173.228	1876.619 ± 58.926	7.529 ± 0.5503	0.4012 ± 0.0796
7027	Na-22	1274.537	888.264 ± 27.625	3.654 ± 0.5266	0.4114 ± 0.1474
7026	Co-60	1332.492	1878.167 ± 58.974	6.784 ± 0.5345	0.3612 ± 0.0848

Table 3.7: HPGe Extrapolated Effeciencies.

Source	Energy	HPGe Eff (%)
Y-88	898	0.7830 ± 0.0471
Y-88	1836.1	0.3119 ± 0.0310

Table 3.8: NaI Extrapolated Effeciencies.

Source	Energy	NaI Eff (%)
Y-88	898	0.6262 ± 0.0246
Y-88	1836.1	0.2158 ± 0.0466

Coincidence Efficiency

Unlike the singles efficiency found above, the efficiency for a coincidence measurement relies on the combined efficiency of both detectors. A known Y-88 source was not available to measure the coincidence activity directly. Instead, the HPGe's geometric efficiency for detecting the Y-88 energy lines at 898 keV and 1836.1 keV was combined with the NaI detectors efficiency for the 1836.1 and 898 keV lines respectively. For example, to obtain the 898 keV coincidence efficiency, the HPGe singles efficiency at this energy line is multiplied by the NaI singles efficiency at the 1836.1 keV line. The uncertainties of the singles efficiency are added in quadrature and the resulting values recorded in column 3 of Table 3.9. The reverse case was applied to find the coincidence efficiency at the 1836.1 keV line and the values are listed in column 3 of Table 3.10.

Table 3.9: HPGe detector efficiency for 898 keV line in coincidence mode.

HPGe Singles 898 keV Eff (%)	NaI Singles 1836.1 keV Eff (%)	HPGe Coincidence Eff (%)
0.7830 ± 0.0471	0.2158 ± 0.0466	0.001690 ± 0.00038

45

Table 3.10: HPGe detector efficiency for 1836.1 keV line in coincidence mode.

HPGe Singles 1836.1 keV Eff (%)	NaI Singles 898 keV Eff (%)	HPGe Coincidence Eff (%)
0.3119 $\pm$ 0.0310	0.6262 $\pm$ 0.0246	0.001953 $\pm$ 0.00021

3.3 Analysis Summary

The following tables summarize the results found in this chapter for singles counting using the amplitude method and coincidence counting using the integral method.

Table 3.11: $T_{1/2}$ and T_{final} results for the 898 keV and 1836.1 energy lines.

Energy	Trig	$T_{1/2}$ (days)	T_{final} (days)
898	sing	127.668 $\pm$ 16.8095	337.209 $\pm$ 22.79
	coin	108.18 $\pm$ 4.89	483.60 $\pm$ 49.74
1836.1	sing	107.273 $\pm$ 17.3321	308.569 $\pm$ 28.79
	coin	100.10 $\pm$ 4.0	305.63 $\pm$ 31.66

Table 3.12: A_0 Analysis results for the 898 keV and 1836.1 energy lines. Efficiency has been applied to the results at time t_{final}.

Energy	Trig	A_0 (Hz) (before efficiency)	A_0 (Hz) (after efficiency)	A(t_{final}) (Hz)
898	sing	2.390 $\pm$ 0.417	305.252 $\pm$ 55.173	34.094 $\pm$ 19.05
	coin	0.0154 $\pm$ 0.0003	912.453 $\pm$ 63.322	39.35 $\pm$ 9.51
1836.1	sing	1.284 $\pm$ 0.1451	411.606 $\pm$ 48.23	55.38 $\pm$ 8.735
	coin	0.0196 $\pm$ 0.0004	1003.32 $\pm$ 44.74	137.594 $\pm$ 29.781

Table 3.13: N_0 analysis results for the 898 keV and 1836.1 energy lines. Efficiency has been applied to the results at time t_{final}.

Energy	Trig	N_0 (nuclei) (before efficiency)	N_0 (nuclei) (after efficiency)	$N(t_{final})$ (nuclei)
898	sing	$(31.77 \pm 5.54) \times 10^6$	$(40.57 \pm 7.33) \times 10^8$	$(4.53 \pm 2.53) \times 10^8$
	coin	$(204.96 \pm 4.20) \times 10^3$	$(121.3 \pm 8.42) \times 10^8$	$(5.23 \pm 1.26) \times 10^8$
1836.1	sing	$(17.06 \pm 1.93) \times 10^6$	$(54.71 \pm 6.41)^8$	$(7.36 \pm 1.16) \times 10^8$
	coin	$(260.44 \pm 5.34) \times 10^3$	$(133.4 \pm 5.95) \times 10^8$	$(18.29 \pm 3.96) \times 10^8$

Chapter 4

Error Analysis

Data measurement and analysis has an inherent amount of error associated with it, and repeated measurements will result in uncertainties. Placement of cuts on the energy spectrum window had an effect on the fit values. It can also reduce noise for coincidence events. Calibrating the detectors is also a source of uncertainty as well as background noise contributions. The following chapter analyzes the contribution of each of these processes to the uncertainty in the reported measurement.

4.1 Linear Fit Systematic Error

The signal is determined by subtracting the underlying background. An estimate of this background is made by fitting the observed count rate with the function below:

$$f(x) = A \int_{\mu-2\sigma}^{\mu+2\sigma} e^{-\frac{1}{2}\left(\frac{x-\mu}{\sigma}\right)^2} dx + Bx + C. \tag{4.1}$$

The above function contains a Gaussian representing the measured signal and a linear function for the background. Figure 4.1 shows an example of the applied fit. The linear fit parameters are used to create a histogram
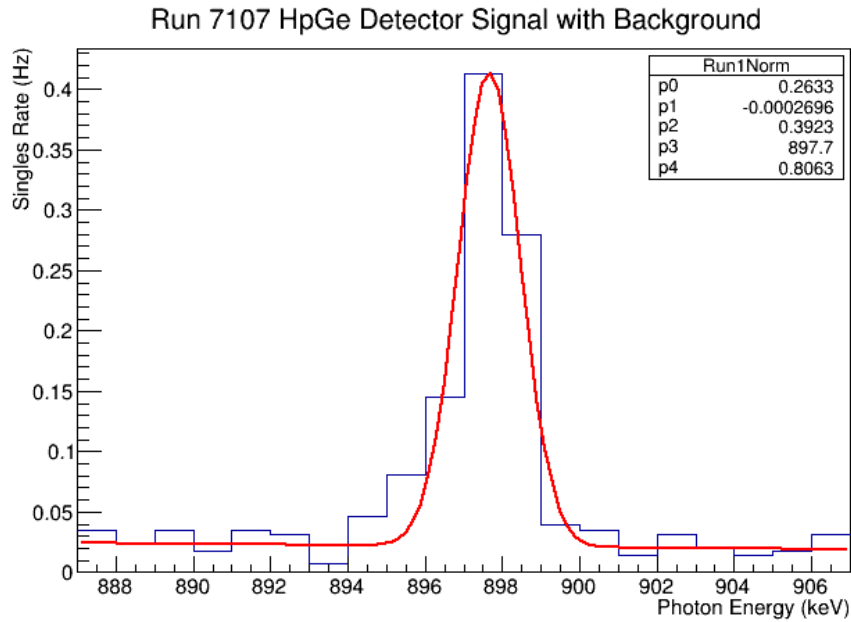
Figure 4.1: Example of a fit to the HPGe 898 keV line for Y-88 decay.

that is subtracted from the raw signal histogram, resulting in a histogram of just a signal. The energy window range used for the fit was adjusted and several fits performed to determine the uncertainty of the fit's slope and y-intercept. This systematic error, based on the fits dependence on the energy window, is shown in the table under the column labeled "Linear Fit of Background". The fit parameters were adjusted to determine the maximum and minimum area of the background. For minimum background area, it was required that the area be positive. The difference between the maximum and unadjusted area value was taken as the positive standard deviation's fluctuation, and the minimum was used for the standard deviation's negative fluctuation. The resulting errors were divided by the signal to obtain a percent error as shown in column 6 of Tables 4.3, 4.4, 4.5, and 4.6. This error dominated for both singles and coincidence counting.

49

4.2   Energy Window Systematic Error

The sample's activity is measured by summing the observed counts over an energy interval. The choice of this integration interval, the energy window, is a source of systematic error. In order to calculate the error associated with the energy window, its range was adjusted based on the statistical variance from a gaussian fit to the background subtracted count rate. The integral was measured for window ranges chosen according to an integer interval of the standard deviation $\mu \pm n\sigma$, where n = 3,4,5. The difference between the largest and mean value was taken as the positive standard deviation, and the lowest was used for the standard deviation negative fluctuation. The resulting errors were divided by the signal to obtain the relative error shown in column 4 of Tables 4.3, 4.4, 4.5, and 4.6.

4.3   Energy Calibration Systematic Error

Prior to each measurement of the Y-88 sample's activity, the detectors were calibrated using several standard sources with known activity and dominant energy lines. This was accomplished by counting certified samples of Cs-137, Co-60, and Na-22, as well as Ba-133 and Mn-54. The observed mean ADC channel number was correlated with the expected energy line from each of the above sources. The correlation was measured using a standard linear fit algorithm. The linear fit algorithm determines the uncertainty of each fit parameter: the slope and the y-intercept. The effects of this uncertainty on the signal was analyzed and is referred to as the energy calibration error.

The uncertainty in the energy calibration just before a singles measurement was used to investigate the impact of the calibration on the measured signal for a given energy window of integration. While the singles measurements took less than 10 minutes, the coincidence measurement re-

quired more than 24 hours. The long term variance of the energy calibration shown in Figure 4.2 was used to estimate the impact of the energy calibration drift during the coincidence measurements. The fit's y-intercept has a temporal variance corresponding to a relative uncertainty of about 1.865%; the slope's relative uncertainty is about 0.608%. The effect of this error on the coincidence signal was analyzed. In both cases, the range of the energy widow is held constant while the slope and the y-intercept were adjusted to account for all possible combinations with and without their respective uncertainty. The integral value was recorded after every fit parameter change and the maximum, minimum, and mean values were obtained. The difference between the largest and mean value was taken as the positive standard deviation, and the lowest was used for the standard deviation's negative fluctuation. The resulting errors were divided by the signal to obtain a percent error as shown in column 5 of Tables 4.3, 4.4, 4.5, and 4.6.

4.4 Systematic Error of the Coincidence Energy Cut

Figure 4.3 shows the coincidence measurements made before (blue) and after (red) energy cuts are applied on the NaI signal to reduce the accidental coincidence events and photons that fail to deposit all their energy in the NaI detector due to compton scattering. The 511 keV line is still present after coincidence requirements, which means it is not accidental. One possibility is the 1836.1 keV photon has enough energy to pair produce. Any photon with energy above 1022 keV has this potential. This would result in two 511 keV photons being created in the detector. Pair production can occur over a short period of time. Since the timing window between the detectors is 200 ns, this is a possible explanation of the 511 keV line, even during coincidence requirements.
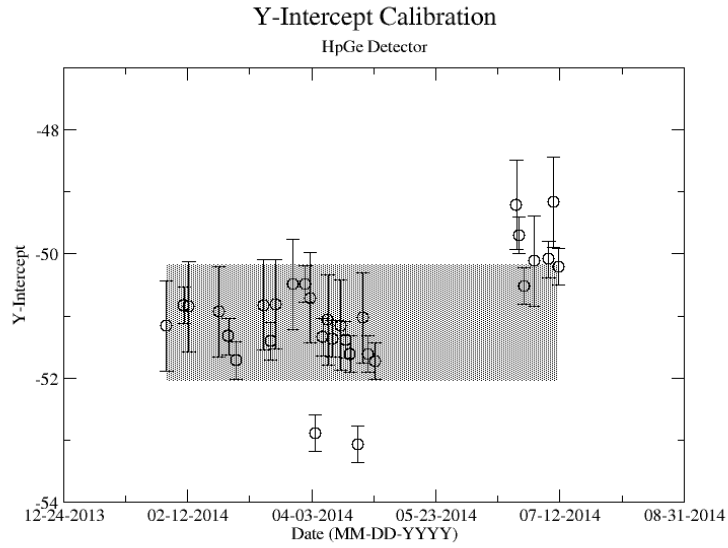
(a) Calibration of the y-intercept. The average y-intercept was -51.1025 +/- 0.9533, represented by the shaded area.
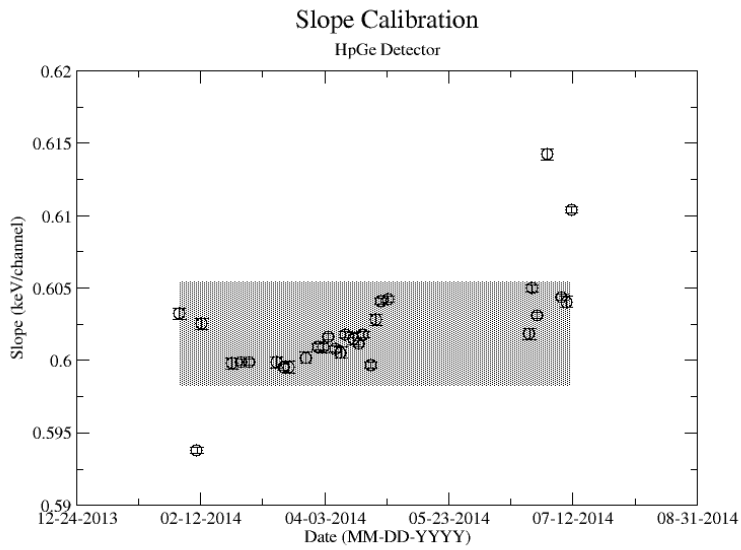
(b) Calibration of the slope. The average slope was 0.6018 +/- 0.0037, represented by the shaded area.

Figure 4.2: Energy calibrations for the HPGe Detector.
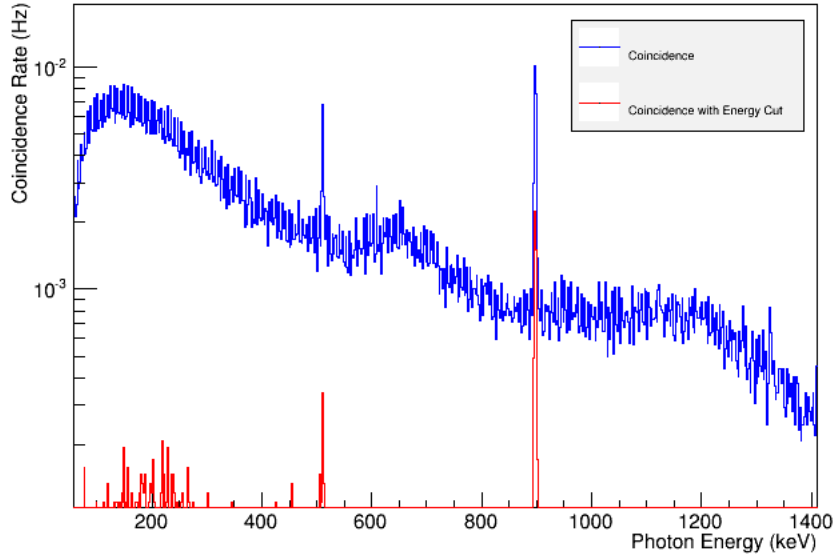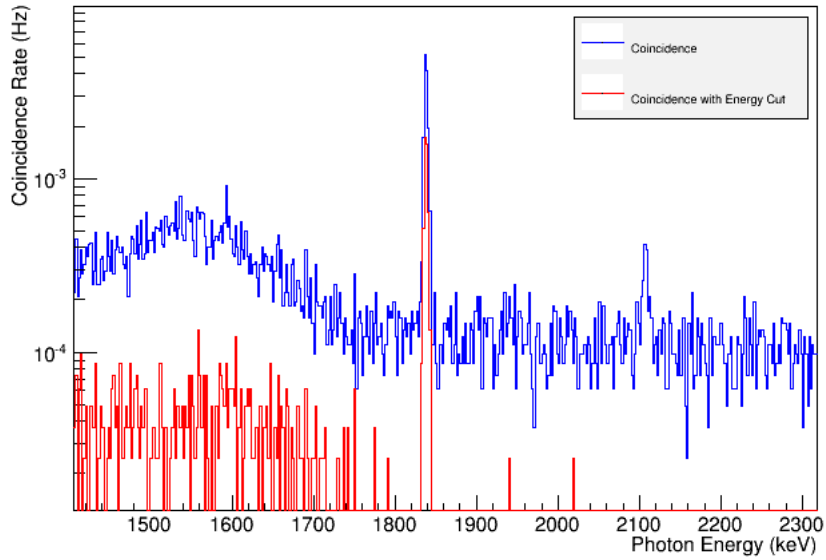
(a) 898 Energy Peak

(b) 1836 Energy Peak

Figure 4.3: Coincidence measurements before (blue) and after (red) energy cuts are applied.

To analyze the error association with coincidence counting only, the signal on the NaI detector was fit to a gaussian distribution. The σ of the gaussian fit was used to adjust the energy cut limits. The energy window was set at lower/upper limit$\pm\sigma$. The integral values were recorded for each instance and the difference between the maximum and unadjusted integral values were taken as the positive standard deviation's fluctuation, while the minimums were used for the standard deviation's negative fluctuation. The resulting errors were divided by the coincidence signal to obtain a percent error as shown in column 8 of Tables 4.4 and 4.6. The limited energy resolution of the NaI detector makes this uncertainty the dominant systematic error. If two HPGe detectors are used, then this uncertainty would decrease substantially to be far less than the remaining dominant systematic error: the energy Gaussian integral uncertainty. This systematic uncertainty is reported, but it is not propagated for the final result to reflect the case of a coincidence apparatus using two HPGe detectors.

4.5   Systematic Error in the SNR

The singles measurement of the 898 keV peak had an initial high background that decays quickly and was more or less constant for singles measurements taken 159 days after irradiation. The large initial background is likely due to activated nuclei with short half lives. This background decreased substantially after about 51 days when the next measurement was taken (the half-life of Y-88 is 106.63 days). The constant background after 51 days reflects the presence of activated material with long half lives. As a result the background for the last three measurements was averaged and used in the denominator for the SNR. The singles background near the 1836 keV line was measured to be around 0.5 Hz and fluctuated less over the experiment compared to the background around the 898 peak.

The coincidence measurements had such little background, due to the nature of the apparatus, that the background was averaged over the first three measurements for both the 898 and the 1836 peaks separately. The background for the final coincidence measurements was ignored, because of the increased noise produced when the detectors nitrogen dewar was filled during the 5 day background measurement. Figure 4.4 shows the background levels during measurement.
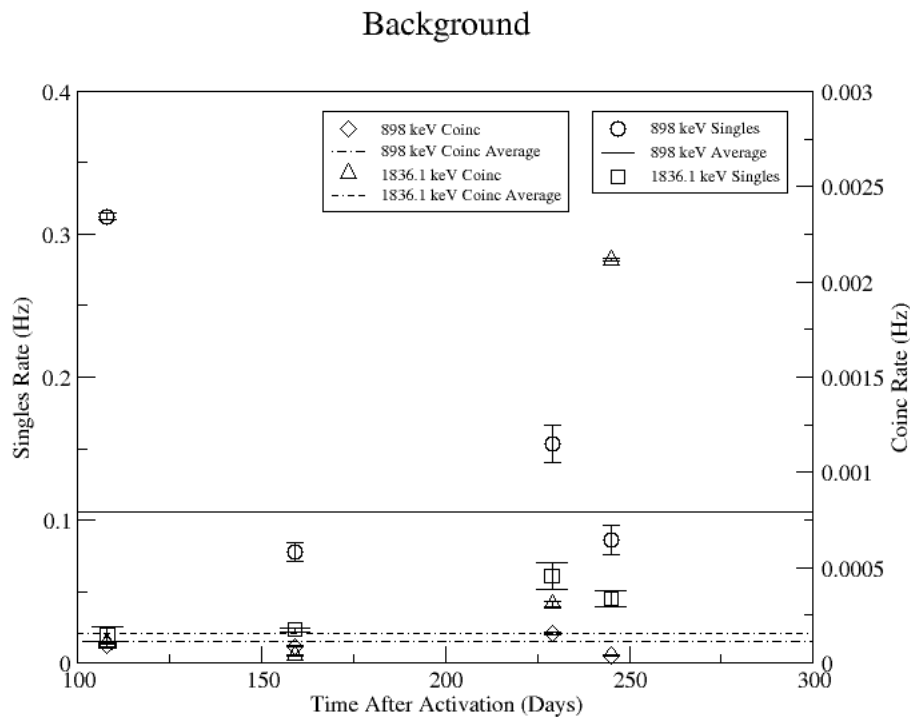
Figure 4.4: Singles and coincidence background observed for several days after activation.

The systematic uncertainty of the background was not analyzed and propagated into the final SNR uncertainty. The signal's total systematic error, described above, was used for the final uncertainty. The background's

systematic error is being ignored.

4.6 Background Contribution to the SNR Error

The analysis of the background uncertainty is described in section 4.1, "Linear Fit Systematic Error." The background's relative statistical uncertainty shown in column 5 of Tables 4.1 and 4.2 is calculated by varying the integral of the background by the uncertainties from the fit and dividing by the background used for the SNR ratio calculation. Column 6 of Table 4.1 presents the uncertainty of the averaged background as mentioned in the previous section. The variance of the coincidence measurement is considerably larger than the individual coincidence measurements. The background in each singles measurement is smaller than the average variance indicating that the individual background measurements could have been made longer to improve their statistical uncertainty.

Table 4.1: 898 keV Background.

Time After Activation (Days)	$(T_{1/2})$	Trig	Background	Linear Fit of Background Error	Statistical Error of Averaged Background
108	1.01	sing	0.3123	$\pm0.801\%$	N/A
		coin	9.518×10^{-5}	$+7.73\%$ -7.45%	$\pm50.01\%$
159	1.49	sing	0.0777	$+8.37\%$ -8.11%	$\pm5.9\%$
		coin	8.732×10^{-5}	$+2.30\%$ -2.28%	$\pm54.51\%$
229	2.15	sing	0.1532	$+8.36\%$ -7.96%	$\pm3.0\%$
		coin	1.554×10^{-4}	$+5.17\%$ -5.06%	$\pm30.63\%$
245	2.30	sing	0.0862	$\pm11.60\%$	$\pm5.3\%$
		coin	3.948×10^{-5}	$+11.24\%$ -11.06%	$\pm120.57\%$

Table 4.2: 1836.1 keV Background.

Time After Activation		Trig	Background	Linear Fit of Background Error	Statistical Error
(Days)	($T_{1/2}$)				
108	1.01	coin	1.037×10^{-4}	$^{+2.42\%}_{-2.39\%}$	$\pm 951.78\%$
159	1.49	coin	4.248×10^{-5}	$^{+8.06\%}_{-7.88\%}$	$\pm 232.34\%$
229	2.15	coin	3.112×10^{-4}	$^{+4.87\%}_{-4.76\%}$	$\pm 317.16\%$
245	2.30	coin	2.114×10^{-3}	$\pm 0.29\%$	$\pm 46.69\%$

4.7   Summary

The following tables contain the values found performing the error analysis described earlier in the chapter. Tables 4.3 and 4.4 are the calculated errors for the 898 keV line for singles and coincidence counting. The calculated errors for the 1836.1 keV line measured in singles and coincidence mode are located in Tables 4.5 and 4.6. The total error was found by adding the column's uncertainties in quadrature. The error from integrating the signal with a gaussian distribution dominated for both singles and coincidence counting. The coincidence events also have a dominate error from applying energy cuts.

It should be noted that this analysis was performed on the results obtained using the integral method outlined in section 3.1. This method failed for singles events to show agreement between the high and low energy lines for the initial values A_0 and N_0. A possible explanation for this method failing is that too much weight is given to the background and driving the initial values from agreement. By requiring coincidence, the background is reduced and the integral method is in agreement with the simple approach used for singles counting.

Table 4.3: Calculated error of 898 kev energy line during singles counting.

Time After Activation (Days)	$(T_{1/2})$	Trig	Energy Window	Energy Calibration	Linear Fit of Background	Gaussian Integration of Signal	Total Systematic Error
108	1.01	sing	+0.367% −0.660%	+1.026% −1.83%	± 0.183%	± 5.132%	+5.32% −5.71%
159	1.49	sing	+0.713% −3.68%	+0.816% −2.438%	+0.747% −0.724%	± 6.29%	+6.52% −8.80%
229	2.15	sing	+32.83% −23.83%	+11.87% −16.35%	+2.7% −2.58%	± 3.68%	+44.94% −40.44%
245	2.30	sing	+1.19% −8.28%	+4.24% −12.0%	± 1.72%	± 10.68%	+12.1% −22.99%

Table 4.4: Calculated error of 898 kev energy line during coincidence counting.

Time After Activation (Days)	$(T_{1/2})$	Trig	Energy Window	Energy Calibration	Linear Fit of Background	Gaussian Integration of Signal	Coincidence Energy	Total Systematic Error	Systematic Error without Coincidence Energy Cut
108	1.01	coin	+0.56% / −0.404%	±0.31%	+0.142% / −0.136%	±3.46%	+10.92% / −33.65%	+12.29% / −34.62%	+3.58% / −3.54%
159	1.49	coin	+0.405% / −0.048%	±0.38%	+0.048% / −0.047%	±1.81%	+9.6% / −14.8%	+10.55% / −15.36%	+1.98% / −1.86%
229	2.25	coin	+0.588% / −3.12%	+1.03% / −2.0%	+0.237% / −0.231%	±3.82%	+14.5% / −31.2%	+16.53% / −36.47%	+4.15% / −6.38%
245	2.30	coin	+0.2% / −0.067%	+0.13% / −0.53%	+0.296% / −0.291%	±0.719%	+24.2% / −101.3%	+24.53% / −102.0%	+0.847% / −0.98%

Table 4.5: Calculated error of 1836.1 kev energy line during singles counting.

Time After Activation		Trig	Energy Window	Energy Calibration	Linear Fit of Background	Gaussian Integration of Signal	Total Systematic Error
(Days)	$(T_{1/2})$						
108	1.01	sing	+0.119% −0.095%	±0.33%	+0.606% −0.582%	±2.34%	+2.46% −2.45%
159	1.49	sing	+0.199% −0.798%	+2.81% −1.42%	±0.279%	±4.79%	+5.66% −5.28%
229	2.15	sing	+10.21% −7.48%	+4.32% −8.65%	+3.26% −3.01%	+11.37% −11.34%	+18.74% −19.94%
245	2.30	sing	+0.245% −5.31%	±1.674%	+2.246% −2.205%	+11.025% −11.107%	+11.414% −13.303%

Table 4.6: Calculated error of 1836.1 kev energy line during coincidence counting.

Time After Activation		Trig	Energy Window	Energy Calibration	Linear Fit of Background	Gaussian Integration of Signal	Coincidence Energy	Total Systematic Error	Systematic Error without Coincidence Energy Cut
(Days)	$(T_{1/2})$								
108	1.01	coin	+0.613% −0.55%	+0.52% −0.5%	±0.04%	±1.45%	+5.02% −41.45%	+6.31% −42.58%	+1.84% −1.79%
159	1.49	coin	+0.435% −0.196%	+0.261% −0.804%	+0.074% −0.073%	±1.267%	+10.07% −61.3%	+10.83% −62.39%	+1.45% −1.62%
229	2.15	coin	+0.629% −2.55%	+1.11% −2.19%	+0.244% −0.239%	±3.44%	+18.71% −93.06%	+20.81% −97.90%	+3.85% −5.85%
245	2.30	coin	+0.125% −0.438%	±0.188%	±0.386%	±7.5%	+28.2% −75.6%	29.5% −76.88%	+7.5% −7.56%

Chapter 5

Results and Conclusion

This thesis set out to quantify the detection limit improvement of coincidence photon activation analysis over the standard photon activation analysis method. Background is one of the most important contributions to establishing a detection limit. One way that a detection limit can be improved is to reduce the background. This can be accomplished by requiring the detection of two photons in coincidence, since the background is typically composed of random events. The detection limit was defined as the point at which the signal could not be distinguished from background. In Chapter 3, the time when the background subtracted signal could no longer be measured (t_{final}) was determine for both PAA and CPAA measurements of the same sample. Using the final time, the information can be converted into a detection limit by calculating the minimum number of activated atoms still detectable in the sample.

5.1   Efficiency for Converting Y-89

The concept of photon activation analysis relies on activating a nucleus by using a high energy photon to eject one or more nucleons (protons or neutrons). The nuclei that have had one or more nucleons removed are

typically unstable and decay. It is well understood that radioactive materials decay as an exponential function of time. We can therefore use the measured signals of the Y-88 sample fitted to an exponential curve to find the initial number of activated atoms in the foil. The exponential fit was extrapolated back to the initial time $t = 0$ when the foil was activated. The half-life of Y-88 is well known, 106.63 days, and was used to calculate the decay constant λ. Using the relationship between activity and the number density, $A = \lambda N$, the initial value, N_0, can be found for time $t = 0$.

The Yttrium foil's mass was found to be 0.0288 +/- 0.0002 g. Using Avogadro's number, N_a, and the isotopic mass of Y-89, $m_i = 88.905848 \frac{g}{mol}$, the number of atoms (N) is found using:

$$N = \frac{m N_a}{m_i}. \tag{5.1}$$

The foil is predicted to contain $(195.1 \pm 1.35) \times 10^{18}$ atoms of Y-89. Taking the ratio of N_0 and the number of atoms will give the accelerator beam's efficiency at activating the sample. Using the above number of atoms and using the average of N_0 for singles and coincidence events, we get a ratio of $(24.42 \pm 5.26) \times 10^{-12}$ using singles and $(65.28 \pm 5.41) \times 10^{-12}$ using coincidence. For every 10^{12} atoms of Y-89, one atom of Y-88 was produced.

5.2 Minimum Number of Y-88 Atoms Detectable

After activating a source, a time will be reached when the sample has decayed past the point where the signal can be identified from the background. The lowest activity of Y-88 that the apparatus could measure is predicted by extrapolating the measured signal to noise ratio forward in time until it is zero. Details on finding the signal to noise ratio can be found in Chapter 3. Beyond this point in time (t_{final}), the signal will not be distinguishable from the background noise and measurements will no longer be

possible with this apparatus. The average value for N_0, $(8.75 \pm 2.02) \times 10^9$, and the time for the SNR to be zero were used in the exponential decay function $N(t) = N_0 e^{-\lambda t}$ to find the lowest measurable activity, $N(t_{final})$, for both energies using singles and coincidence counting. For the 898 keV energy line, $N(t_{final})$ was $(9.77 \pm 2.35) \times 10^8$ after 337.209 days for singles and $(3.77 \pm 0.954) \times 10^8$ after 483.60 days for coincidence counting. For the 1836.1 keV energy line, $N(t_{final})$ was $(11.77 \pm 2.93) \times 10^8$ after 308.569 days for singles counting. For this apparatus, coincidence counting can measure half of the singles minimum number of detectable atoms. The detection limit can be improved by at least a factor of two using coincidence counting over standard PAA.

Appendix A

Elemental Analysis Methods

The atomic methods listed in Table 1.1 are briefly described in the following sections.

A.1 Inductively Coupled Plasma Atomic Emission Spectroscopy (ICP-AES)

Inductively Coupled Plasma Atomic Emission Spectroscopy (ICP-AES) [12] is sometimes referred to as ICP-OES, meaning optical emission spectrometry. ICP-AES utilizes the ICP plasma to produce excited atoms and ions that will emit electromagnetic radiation at wavelengths characteristic of a particular element. The concentrations of the elements within a sample can be determined based on the intensity of the emissions. The ICP-AES is composed of an ICP and the optical spectrometer. A liquid or organic sample is injected into the hot plasma torch, where compounds are usually completely dissociated. The excited atoms and ions emit radiation at characteristic lines, which are focused onto a diffraction grating and slit system, where it is dispersed into its component wavelengths in the optical spectrometer. The photomultiplier tubes used by previous systems to

measure the light intensity have been replaced in modern systems by an array of semiconductor photodetectors such as solid state charge-coupled devices (CCDs). The intensity of each line is compared to previously measured intensities of known concentrations of the elements in order to calibrate the system. ICP-AES has been used to measure trace metal concentrations ranging from 10^{-4} to 1 ppm [4].

A.2   Atomic Absorption Spectrometry (multi-element AAS)

Atomic Absorption Spectrometry (AAS) [4] is a spectra-analytical procedure used for the determination of elements to within $1 \rightarrow 100$ ppm using the absorption of optical radiation by the atoms. AAS can be used to determine over 70 different elements in solution, but the technique can only measure one element at a time. In order to analyze an element, a liquid sample must be atomized into a vapor. The most common atomizers are flames and electrothermal graphite tube atomizers. Since AAS's basic mode of operation is absorption, as opposed to emission, optical radiation characteristic of the element to be determined is passed through the sample vapor. A hollow cathode lamp is the most common radiation source in AAS. The radiation then passes into a monochromator, either a prism or diffraction grating, followed by a slit in order to separate the element-specific radiation from any other radiation emitted by the radiation source. The optical radiation is detected by a photomultiplier detector.

A.3   Particle-Induced X-ray Emission (PIXE)

Particle-induced X-ray Emission (PIXE) [4] is a non-destructive analytical technique used in determining surface elemental composition of a mate-

rial or sample. It has detection limits typically ranging from 0.5 to 5 ppm and 1 to 20 ppm for μPIXE [13]. The particle beam most often used for PIXE is a positive ion beam. Three types of spectra can be collected using PIXE: X-ray emission spectrum, Rutherford backscattering spectrum, and proton transmission spectrum. The proton beam strikes a sample, and causes inner shell vacancies. The outer shell electrons de-excite to replace, or fill, the inner shell vacancies, emitting radiation in the X-ray portion of the electromagnetic spectrum. The energy of the emitted photon is characteristic of the atom. These emissions are detected using X-ray detectors like Si(Li) detectors and silicon drift detectors. Protons in the ion beam will also experience elastic collisions, Rutherford backscattering, with the nucleus of the atom. The backscatter can give composition information on the sample and allow for a correction when the X-ray photon is lost within the sample.

A.4   X-ray Fluorescence Spectrometry (XRF)

X-ray Fluorescence Spectrometry (XRF) is an analytical technique used for elemental analysis, particularly in the investigation of metals, glass, and ceramics. In XRF, the primary X-Rays are most commonly produced by an X-ray tube and have detection limits around $10 \rightarrow 100$ ppm [14]. However, alternative primary sources include synchrotron radiation, with reported detection limits of 100 ppm or better, can be used [15]. A synchrotron is a large electron accelerator which produces electromagnetic radiation across the whole spectrum, with high spectral purity and high beam intensity. Desired sections of the spectrum can be selected by bending the beam. The beam is de-accelerated and in order to conserve energy, a photon will be emitted. This beam can then be used as the primary beam in XRF analysis. Once the primary X-rays strike the solid sample, two processes occur: scattering and absorption. Vacancies are created in the orbital shell of

the sample atoms as a result of energy absorption and the ejection of an electron. The removal of an electron makes the structure of the atom unstable, and electrons in higher orbitals will de-excite to the lower orbital to fill the vacancy. During this transition, radiation is emitted with energy characteristic of the atom present. This secondary radiation from the sample can be analyzed with two different approaches, energy-dispersive or wavelength-dispersive analysis. In energy-dispersive analysis, various types of solid state detectors are used to collect the incoming X-ray photon, while wavelength-dispersive analysis employs a monochromator and a photomultiplier for detection of a single wavelength of radiation.

A.5   Inductively Coupled Plasma Mass Spectrometry (ICP-MS)

Inductively Coupled Plasma Mass Spectrometry (ICP-MS) [16] is an elemental analytical technique that combines a high-temperature ICP plasma with a mass spectrometer. A sample is introduced into the ICP, typically as an aerosol, where it ionizes the sample's atoms. The resulting ions are positively charged, which means they can be focused by electrostatic lenses into a mass spectrometer. Quadrupole mass filters are the most common type of mass spectrometers. This type uses four rods with alternating AC and DC voltages to permit ions of a single mass-to-charge ratio to pass through. Since different isotopes of a single element have different masses, filtering ions this way means ICP-MS can also supply isotopic information. Once the ions have been separated by their mass-to-charge ratio, they are detected. A channel electron multiplier (CEM) was used in early ICP-MS instrumentation; however, the open glass cone coated with a semi-conductor has since been replaced with discrete metal dynode type detectors [17]. The ICP-MS system has detection limits that range from 10^{-7} to 0.001 parts-per-million (ppm) [18].

Appendix B

Calibration Source Certificates

The certificates for standard sources of Cs-137, Co-60, Na-22, Ba-133, and Mn-54 used for calibrating detectors.

CERTIFICATE OF CALIBRATION

MODEL CAL2600 GAMMA STANDARD

Radionuclide:	Cs-137	**Activity:**	3.408 kBq (92.11 nCi)
Serial Number:	129792	**Reference Date:**	1200 PDT July 1, 2008
Half Life[1]:	30.0 ± 0.2 years		

PRINCIPAL EMISSIONS[1]

Type	Energy (keV)	Intensity (%)
gamma	661.660	85.21

SOURCE DESCRIPTION

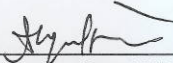|			
Active Diameter:	1 mm	**Backing:**	1 mm plastic
Overall Diameter:	25.4 mm	**Cover:**	1 mm plastic
Thickness:	3.2 mm		

METHOD OF CALIBRATION

The source was calibrated on a high purity germanium detector using a Cs-137 efficiency at 661.660 keV. This efficiency was established and verified through ongoing intercomparisons with the National Institute of Standards and Technology. This standard is indirectly (implicitly) traceable to the National Institute of Standards and Technology.

North American Scientific, Inc. actively participates in the Radioactivity Measurements Assurance Program conducted by the National Institute of Standards and Technology in cooperation with the Nuclear Energy Institute.

TOTAL UNCERTAINTY (99% Confidence Level)

Systematic uncertainty	3.00%
Random uncertainty	0.92%
Total uncertainty (quadratic sum)	± 3.14%

_____
Seyed Miri
Calibration Laboratory Manager

June 30, 2008
Date

REFERENCES

(1) Table of Radioactive Isotopes, 7th edition, 1986.

• LEAK TEST CERTIFICATION ON REVERSE •

20200 Sunburst Street, Chatsworth, CA 91311 • PH: (818) 734-8600 • Fax: (818) 734-5200

north american
SCIENTIFIC

C-0000918

71

CERTIFICATE OF CALIBRATION

MODEL CAL2600 GAMMA STANDARD

Radionuclide:	Co-60	**Activity:**	3.994 kBq (108.0 nCi)
Serial Number:	124838	**Reference Date:**	1200 PDT June 1, 2008
Half Life[1]:	5.271 ± 0.001 years		

PRINCIPAL EMISSIONS[1]

Type	Energy (keV)	Intensity (%)
gamma	1173.237	99.90
gamma	1332.501	99.9824

SOURCE DESCRIPTION

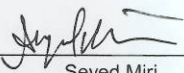|			
Active Diameter:	1 mm	**Backing:**	1 mm plastic
Overall Diameter:	25.4 mm	**Cover:**	1 mm plastic
Thickness:	3.2 mm		

METHOD OF CALIBRATION

The source was calibrated on a high purity germanium detector using a Co-60 efficiency at 1173.237 keV. This efficiency was established and verified through ongoing intercomparisons with the National Institute of Standards and Technology. This standard is indirectly (implicitly) traceable to the National Institute of Standards and Technology.

North American Scientific, Inc. participates in the Radioactivity Measurements Assurance Program conducted by the National Institute of Standards and Technology in cooperation with the Nuclear Energy Institute.

TOTAL UNCERTAINTY (99% Confidence Level)

Systematic uncertainty	3.00%
Random uncertainty	0.93%
Total uncertainty (quadratic sum)	± 3.14%

_____
Seyed Miri
Calibration Laboratory Manager

May 27, 2008
Date

REFERENCES

(1)   Table of Radioactive Isotopes, 7th edition, 1986.

•LEAK TEST CERTIFICATION ON REVERSE•

72

CERTIFICATE OF CALIBRATION

MODEL CAL2600 GAMMA STANDARD

Radionuclide:	Na-22	**Activity:**	4.014 kBq (108.5 nCi)
Serial Number:	129741	**Reference Date:**	1200 PDT July 1, 2008
Half Life[1]:	2.602 ± 0.002 years		

PRINCIPAL EMISSIONS[1]

Type	Energy (keV)	Intensity (%)
gamma	1274.53	99.937
annihilation gamma	511	178.8

SOURCE DESCRIPTION

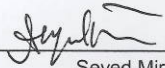|			
Active Diameter:	1 mm	**Backing:**	1 mm plastic
Overall Diameter:	25.4 mm	**Cover:**	1 mm plastic
Thickness:	3.2 mm		

METHOD OF CALIBRATION

The source was calibrated on a high purity germanium detector using a Na-22 efficiency at 1274.53 keV. This efficiency was established and verified through ongoing intercomparisons with the National Institute of Standards and Technology. This standard is indirectly (implicitly) traceable to the National Institute of Standards and Technology.

North American Scientific, Inc. participates in the Radioactivity Measurements Assurance Program conducted by the National Institute of Standards and Technology in cooperation with the Nuclear Energy Institute.

TOTAL UNCERTAINTY (99% Confidence Level)

Systematic uncertainty	3.00%
Random uncertainty	0.81%
Total uncertainty (quadratic sum)	± 3.11%

_____   July 2, 2008
          Seyed Miri   Date
Calibration Laboratory Manager

REFERENCES

(1)   Table of Radioactive Isotopes, 7th edition, 1986.

• LEAK TEST CERTIFICATION ON REVERSE •

CERTIFICATE OF CALIBRATION

MODEL CAL2600 GAMMA STANDARD

Radionuclide:	Ba-133	**Activity:**	4.529 kBq (122.4 nCi)
Serial Number:	129789	**Reference Date:**	1200 PDT July 1, 2008
Half Life[1]:	10.54 ± 0.03 years		

PRINCIPAL EMISSIONS[1]

Type	Energy (keV)	Intensity (%)
gamma	80.989	34.2
gamma	276.388	7.09
gamma	302.851	18.4
gamma	355.999	62.2
gamma	383.841	8.92

SOURCE DESCRIPTION

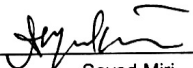|			
Active Diameter:	1 mm	**Backing:**	1 mm plastic
Overall Diameter:	25.4 mm	**Cover:**	1 mm plastic
Thickness:	3.2 mm		

METHOD OF CALIBRATION

The source was calibrated on a high purity germanium detector using a Ba-133 efficiency at 355.999 keV. This efficiency was established and verified through ongoing intercomparisons with the National Institute of Standards and Technology. This standard is indirectly (implicitly) traceable to the National Institute of Standards and Technology.

North American Scientific, Inc. participates in the Radioactivity Measurements Assurance Program conducted by the National Institute of Standards and Technology in cooperation with the Nuclear Energy Institute.

TOTAL UNCERTAINTY (99% Confidence Level)

Systematic uncertainty	3.00%
Random uncertainty	0.93%
Total uncertainty (quadratic sum)	± 3.14%

_____   June 30, 2008
Seyed Miri   Date
Calibration Laboratory Manager

REFERENCES

(1)   Table of Radioactive Isotopes, 7th edition, 1986.

• LEAK TEST CERTIFICATION ON REVERSE •

20200 Sunburst Street, Chatsworth, CA 91311 • PH: (818) 734-8600 • Fax: (818) 734-5200

north american SCIENTIFIC

C-0000918

CERTIFICATE OF CALIBRATION

MODEL CAL2600 GAMMA STANDARD

Radionuclide:	Mn-54	**Activity:**	4.086 kBq (110.4 nCi)
Serial Number:	129804	**Reference Date:**	1200 PDT July 1, 2008
Half Life[1]**:**	312.20 ± 0.07 days		

PRINCIPAL EMISSIONS[1]

Type	Energy (keV)	Intensity (%)
gamma	834.826	99.975

SOURCE DESCRIPTION

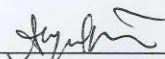|			
Active Diameter:	1 mm	**Backing:**	1 mm plastic
Overall Diameter:	25.4 mm	**Cover:**	1 mm plastic
Thickness:	3.2 mm		

METHOD OF CALIBRATION

The source was calibrated on a high purity germanium detector using a Mn-54 efficiency at 834.826 keV. This efficiency was established and verified through ongoing intercomparisons with the National Institute of Standards and Technology. This standard is indirectly (implicitly) traceable to the National Institute of Standards and Technology.

North American Scientific, Inc. participates in the Radioactivity Measurements Assurance Program conducted by the National Institute of Standards and Technology in cooperation with the Nuclear Energy Institute.

TOTAL UNCERTAINTY (99% Confidence Level)

Systematic uncertainty	3.00%
Random uncertainty	0.91%
Total uncertainty (quadratic sum)	± 3.14%

_____
Seyed Miri
Calibration Laboratory Manager

June 30, 2008
Date

REFERENCES

(1)   Table of Radioactive Isotopes, 7th edition, 1986.

• LEAK TEST CERTIFICATION ON REVERSE •

Appendix C

ROOT Script Examples

1. Normalize the data using the length of collection:

```
void AW_Norm(Float_t t)
{

  TH1F *run1Hist=new TH1F("run1Hist","run1Hist",4400,0,4400);

  ntuple->Draw("ADC7*0.599803-50.9271 >>run1Hist","ADC3>670 && ADC3<
790");

  TH1F *Run1Norm=new TH1F("Run1Norm","Run1Norm",4400,0,4400);

  Run1Norm->Add(run1Hist,1);
  Run1Norm->Scale(t);
  Run1Norm->Draw();

}
```

2. Subtracting the background noise from signal:

```
void BackgroundSub(Float_t p0, Float_t p1, Float_t t)
{

  TH1F *coin1=new TH1F("coin1","coin1",20,1825,1845);

  ntuple->Draw("ADC7*0.599803-50.9271 >>coin1","ADC3>670 && ADC3<
790");


  TH1F *lin1=new TH1F("lin1","lin1",20,1825,1845);

  for(int i=1825;i<1846;i++){
    lin1->Fill(i,p0+p1*i);
      }

  TH1F *sub=new TH1F("sub1","sub1",20,1825,1845);

  sub1->Add(coin1,t);
  sub1->Add(lin1,-1);
  sub1->Draw();

}
```

Bibliography

[1] IAEA. *Photon Activation Analysis as a Complementary Technique for Supporting Applications in Environmental Research*, January 2012.

[2] C.R. Segebade; H.P. Weise; G.J. Lutz. *Photon Activation Analysis*. Walter de Gruyter, Berlin, New York, 1988.

[3] George J. Lutz. Photon Activation Analysis-A Review. *ANALYTICAL CHEMISTRY*, 43(1), January 1971.

[4] A. Mark Pollard; Carl Heron. *Archaeological Chemistry*. Royal Society of Chemistry, 2nd edition, 2008.

[5] Michael D. Glascock. Overview of Neutron Activation Analysis.

[6] NNDC Chart of Nuclides. Adopted Levels, Gammas for Sr88.

[7] NNDC Chart of Nuclides. Gamma coincidence data.

[8] NNDC Chart of Nuclides. Y-88 level scheme.

[9] Kenneth S. Krane. *Introductory Nuclear Physics*. Wiley, 3rd edition, October 1987.

[10] CERN. Root data analysis framework.

[11] *Nuclides and Isotopes Chart of the Nuclides*. Knolls Atomic Power Laboratory, 17 edition, 2010.

[12] J.M. Mermet. Is it still possible, necessary and beneficial to perform research in ICP-atomic emission spectrometry? *Journal of Analytical Atomic Spectrometry*, 20:11–16, November 2005.

[13] John L. Campbell; William J. Teesdale; Norman M. Halden. Theory, Practice and Application of Mirco-PIXE Analysis and Element-Distribution Maps. *The Canadian Mineralogist*, 33:279–292, 1995.

[14] Balwant Singh; Markus Gräfe. *Synchrotron-based Techniques in Soils and Sediments*, volume 34. Elsevier, 1st edition, February 2010.

[15] Robin Gill. *Modern Analytical Geochemistry: An introduction to Quantitive Chemical Analysis for Earth, Environmental and Materials Scientists*. Pearson Education Limited, 1997.

[16] Ruth E. Wolf. What is ICP-MS? ... and more importantly, what can it do?, March 2005.

[17] Robert Thomas. Spectroscopy Tutorial: A Beginner's Guide to ICP-MS, Part X - Detectors. *Spectroscopy*, pages 34–39, April 2002.

[18] Jonathan Knowls. Inductively Coupled Plasma Mass Spectrometry ICP-MS.